

Chapter

1 Introduction

1.1 Background and motivation

This thesis presents an investigation of the modelling and optimal design of a particular topology of 3-degree-of-freedom (DOF) $XY\theta_Z$ micro-motion stage. This stage provides micron-scale motion in X and Y directions and a rotation about the Z-axis. Such a stage can be used for applications where positioning of components with micrometre, or even nanometre positioning accuracy is required. Some applications are; the positioning of samples in a scanning-electron-microscope; the positioning of masks in lithography; aligning fibre-optics and lasers; and manipulation of micro-scale objects in micro-biology or micro-systems assembly.

Over the last 30 years numerous systems have been developed to perform a vast range of micro-positioning tasks. These systems have used many different methods to provide this fine-accuracy motion. To provide the finest-accuracy motion the most commonly used core components of micro-motion stages are unique fine resolution actuators and compliant mechanisms. Piezoelectric, electromagnetic, electrostatic and shape memory alloy actuators can be displaced by an almost limitlessly small amount. Of these, piezoelectric actuators are the most common. Their resolution is

limited only by the quality of the voltage signal applied to them and the capability of the sensors used to detect the motion; sub-nanometre resolution is achievable. Compliant mechanisms are mechanisms that provide force and motion transfer via elastic deformation of members rather than using components such as revolute joints. Compliant mechanisms are commonly machined from a single piece of material. The combination of fine resolution actuators and compliant mechanism means that the system possesses no gears, bearings or sliding surfaces and is therefore free of backlash and Coulomb friction. Therefore the position resolution possible is limited only by the actuators and the position sensors and thus position resolution of sub-nanometres is possible.

The $XY\theta_z$ micro-motion stage investigated in this study uses a particular topology of monolithic compliant mechanism and three stack piezoelectric actuators, hereafter referred to as piezo-actuators. The compliant mechanism used is a 3RRR (three revolute-revolute-revolute) flexure hinge based parallel compliant mechanism. A parallel mechanism is one that has closed kinematic chains. This parallel mechanism uses three RRR linkages. Each of the three RRR linkages uses three circular profile notch flexure hinges. Each flexure hinge provides predominantly rotational motion about one axis. One such mechanism is shown in Figure 1-1.

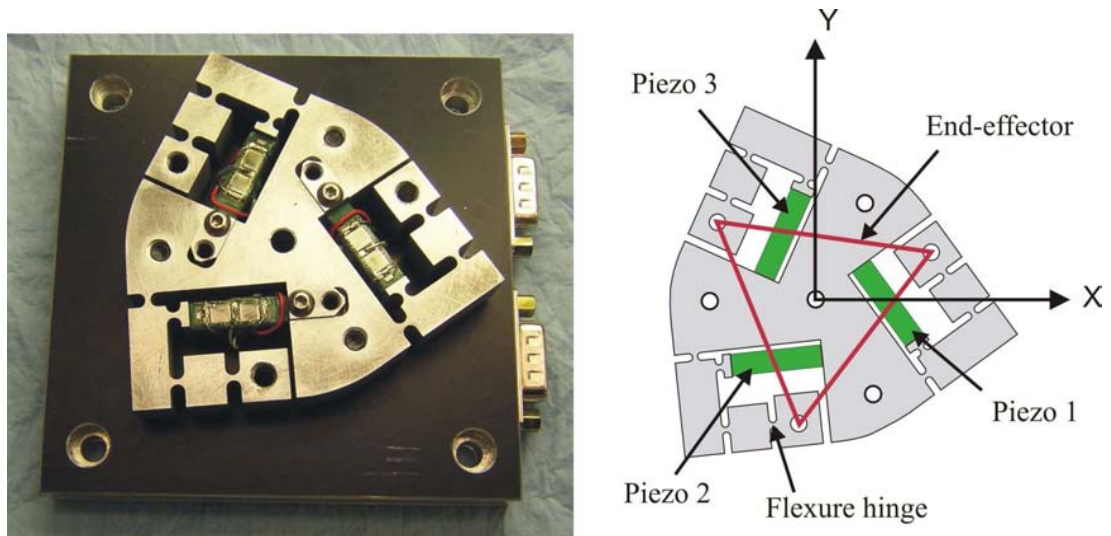


Figure 1-1 - A flexure hinge based 3RRR compliant mechanism and piezo-actuators, without end-effector; and a schematic diagram showing where the end-effector is mounted.

This topology of mechanism has numerous advantages that make it suited to micro-motion applications. It shares the widely acknowledged benefits of all parallel mechanisms such as; high rigidity; high accuracy motion; light link mass, as the actuators are located in the base; and high resonant frequency. These advantages make parallel mechanisms better suited to high accuracy and high speed applications than serial mechanisms. A schematic of serial and parallel 3-DOF mechanisms can be seen in Figure 1-2 to clarify the difference between them.

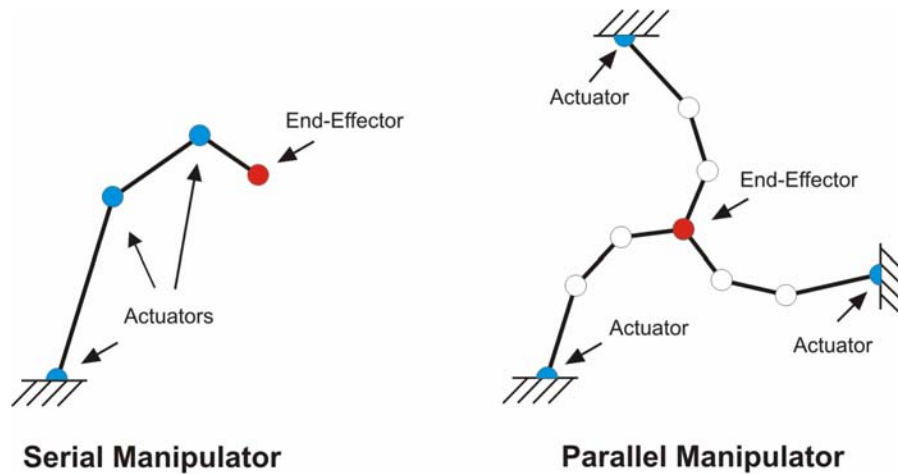


Figure 1-2 – Schematic diagram of a serial and parallel 3-DOF mechanism.

In addition to the advantages common to all parallel mechanisms, the 3RRR topology has advantages due to its symmetrical design. It is less susceptible to kinematic variations with change of temperature; it can provide $XY\theta_Z$ motion with a very simple and light weight structure; it can provide uncoupled stiffness between the actuators; and it can have a symmetrical workspace.

As yet the 3RRR topology of compliant mechanism has not been widely applied in the design of micro-motion stages. Research has been conducted by a variety of research groups to investigate this design and its application. While a $XY\theta_Z$ stage using similar topology has been developed by the company Dynamic Structures and Materials, Franklin, TN, USA [Lobontiu, 2002(c)].

To design a micro-motion stage using a compliant mechanism kinematic and dynamic models of the compliant mechanism are needed. The behaviour of compliant mechanisms is different to the well understood rigid-body mechanism.

New modelling approaches have been developed in conjunction with the micro-motion stages to aid their design. There are a number of modelling methods that have been applied to model the 3RRR compliant mechanism, but as yet there is not a clear understanding as to how well these approaches work for this particular topology of compliant mechanism. A detailed investigation of the modelling of the 3RRR compliant mechanism is presented in this thesis.

To design a micro-motion stage to best satisfy given design requirements an optimal design approach should be taken. This requires an accurate model of the complete stage, consisting of compliant mechanism and piezo-actuators. However, many previous optimal design approaches have considered the compliant mechanism model only. In addition, to allow for fast convergence to an optimal design this model should be computationally efficient. A good understanding of the relationship between micro-motion stage parameters and the stage performance is also useful, as then design rules can be established that can simplify the design process and aid the design optimisation. This can be achieved by performing a parametric study of the micro-motion stage. A detailed parametric study of a micro-motion stage using the 3RRR compliant mechanism has not been presented in the current literature, and so it is presented in this thesis. The optimal design of a micro-motion stage using a compliant mechanism similar to the 3RRR topology has only been addressed once in the current literature, for a single specific case [Ryu, 1997]. Furthermore, this optimal design approach did not consider the total micro-motion stage, but only considered the compliant mechanism. The development of an optimal design approach for the $XY\theta_z$ micro-motion stage is presented in this thesis.

1.2 Objectives and scope

This study has two major objectives. The first is to investigate modelling methods that can be used to model the 3RRR compliant mechanism kinematics and dynamics. The study will establish how well each of these performs. The model is needed for optimal design and therefore an accurate yet computationally simple model is desirable. Therefore computational efficiency is an important criterion to be considered. In addition the modelling of the piezo-actuators is also considered and incorporated into the model to give a more complete $XY\theta_Z$ micro-motion stage model.

The second objective is to develop an optimal design approach so that an $XY\theta_Z$ micro-motion stage, using the 3RRR compliant mechanism, can be designed to satisfy any given, but achievable, performance requirements. A parametric study is performed first, and from this design rules are established, so that the optimisation procedure can be simplified.

The study is limited to consideration of the 3RRR topology compliant mechanism using right-circular notch flexure hinges. Commonly used analytical equations are used in some models to model the flexure hinges. This means that the accuracy of these models is limited by the accuracy of the equations. The 3RRR compliant mechanism is a planar mechanism and in this study all the models only consider in-plane motions. Therefore, only two-dimensional (2-D) models are used.

1.3 Methodology

1.3.1 Compliant mechanism modelling

Three modelling methods to derive the kinematics and dynamics of the 3RRR compliant mechanism are presented and compared. The first model presented is an analytical model developed using *Maple* software, and also implemented in Matlab. This uses a linear approach to derive the commonly used Pseudo-Rigid-Body-Model (PRBM). This model assumes that the flexure hinges are purely revolute joints with stiffness, joined by rigid links. An analytical equation is used to determine the flexure hinge bending stiffness. The other two models are numerical models developed using ANSYS. The first numerical model is a commonly used 2-D Finite-Element-Model (FEM). The second numerical model assumes the flexure hinges to have three planar degrees-of-freedom and uses analytical equations to determine the stiffness in each of these. The links are assumed to have some flexibility. This model has been termed the Simple-Compliant-Hinge-Model (SCHM). These methods were used to model a single flexure hinge, a compliant four-bar linkage and a particular design of 3RRR compliant mechanism. A prototype of the 3RRR compliant mechanism, as shown in Figure 1-1, was manufactured and used in experimental verification of the models. This 3RRR compliant mechanism was developed by [Wang et al., 1997] and has been further studied by [Zou, 2000] and [Zhang, 2002]. This investigation revealed a number of failings of this design and design improvements were suggested.

1.3.2 $XY\theta_Z$ micro-motion stage modelling

Modelling of the piezo-actuators is also considered and included into all three models to give more complete $XY\theta_Z$ micro-motion stage models. A simple linear piezo-actuator model is used as a first approximation of the piezo-actuator behaviour. Using the $XY\theta_Z$ stage models, the workspace, coupling and natural frequency are investigated. The workspace of the stage is presented in detail, which gives new understanding of the workspace shape, size and orientation. Two distinct workspace areas are defined, these are the reachable and constant-orientation workspaces.

1.3.3 Optimal design procedure

So that the relationship between design parameters and stage performance can be better understood a parametric study is conducted. This parametric study highlights some useful relationships that are used to establish design rules to aid the optimal design of the $XY\theta_Z$ micro-motion stage. Both the PRBM and SCHM modelling methods are used and compared. This establishes which method is most appropriate for use in optimal design. An optimal design approach is then applied to design a $XY\theta_Z$ micro-motion stage to be used in an application in a Scanning-Electron-Microscope (SEM). Models of the optimal design are created using the PRBM, SCHM and 2-D FEM methods so that they can be compared. A prototype of this optimal design is then manufactured and used to experimentally validate these models.

1.4 Organisation of thesis

A literature review is presented in Chapter 2. In Chapter 3 the linear analytical modelling method is presented and a PRBM of the 3RRR compliant mechanism is developed. In Chapter 4 the numerical modelling methods are presented and models of the 3RRR compliant mechanism are developed and compared. In Chapter 5 the 3RRR compliant mechanism models are combined with a piezo-actuator model to give a $XY\theta_z$ stage model and these models are compared. A parametric study of the 3RRR compliant mechanism model and $XY\theta_z$ stage model is conducted in Chapter 6. In Chapter 7 an optimal design approach is applied to the $XY\theta_z$ stage model and three models of the optimal design are compared. In Chapter 8 an experimental investigation of the two prototype stages is presented and the results used to validate the models. The conclusions and suggestions for future work are presented in chapter 9.

Chapter

2 Literature review

This chapter provides a thorough review of the literature relating to the modelling and optimal design of micro-motion stages using the 3RRR topology compliant mechanism. An overview of micro-motion stages and compliant mechanism modelling, in general, is given, as is an in depth discussion of notch flexure hinge modelling. The modelling of piezo-electric actuators for inclusion into micro-motion stage models is also considered in depth. The optimal design of micro-motion stages, in general, is discussed, with particular attention given to optimal design of the 3RRR topology compliant mechanism. Finally, the gaps in current knowledge are identified, providing the direction of this current research.

2.1 Micro-motion stages overview

Micro-motion stages have been developed over the last 25 years to perform a multitude of tasks. Micro-motion stages are also commonly referred to as micro-manipulators or micro-positioners, depending on the application for which they are designed. In this discussion the term micro-motion stage will be used to refer to all the systems designed to provide micro-scale motion. Some applications in which they are used are; the manipulation of microscopic objects in biotechnology or

micro-systems assembly operations; manoeuvring masks in micro-lithography; moving the scanning tip in scanning probe microscopy (SPM) or moving samples in a scanning electron microscope; the alignment of fibre optic cables; micro-surgery operations; and even the precision control of tools used in CNC machining operations.

Micro-motion stages have been developed using a variety of actuators and motion and force transfer mechanisms. To provide the finest-accuracy motion the most commonly used core components of micro-motion stages are unique fine resolution actuators and compliant mechanisms. Piezoelectric, electromagnetic, electrostatic and shape memory alloy actuators have all been used as they can potentially be displaced with sub-nanometre resolution. Compliant mechanisms provide motion and force transfer via elastic deformation of the mechanism rather than using revolute or other types of joints. Many compliant mechanisms are monolithic, being manufactured from a single piece of material. Many derive their compliance using notch flexure hinges, as shown in Figure 2-1. The combination of fine resolution actuators and compliant mechanism means that the system possesses no gears, bearings or sliding surfaces and is therefore free of backlash and Coulomb friction. Therefore the position resolution possible is limited only by the actuators and the position sensors and thus position resolution of sub-nanometres is possible.

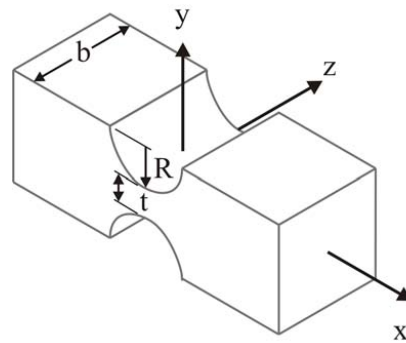


Figure 2-1 - Schematic of a circular profile notch flexure hinge.

Scire and Teague (1978) developed one of the first documented micro-motion stages, which used a monolithic, planar compliant mechanism with circular flexure hinges, and was driven by a piezo-actuator. This 1-DOF amplifying stage, which is shown in Figure 2-2, was used in an electron microscope.

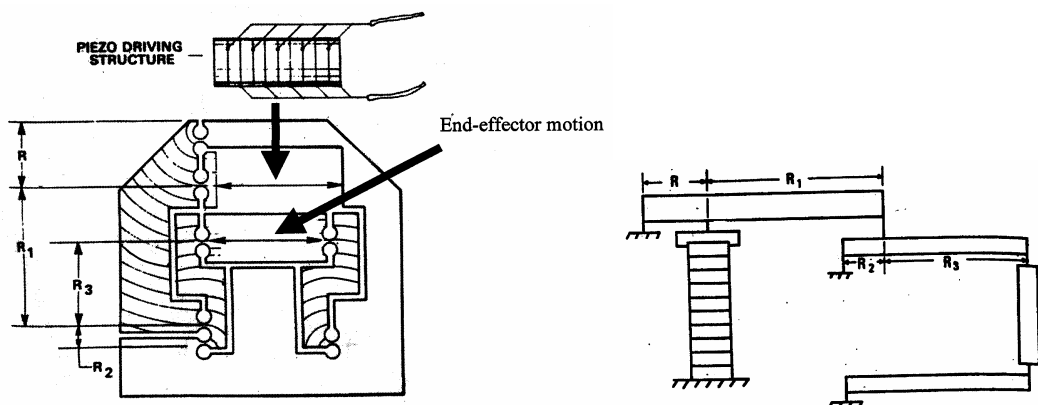


Figure 2-2 - Schematic of the 1-DOF compliant stage developed by Scire and Teague (1978) and an equivalent lever structure.

Since then numerous micro-motion stages using compliant mechanisms have been developed, some of which can provide multiple-DOF motion. An example of a 6-DOF stage using a Stewart platform is shown in Figure 2-3.

NOTE: This figure is included on page 14 of the print copy of the thesis held in the University of Adelaide Library.

Figure 2-3 - 6-DOF Micromanipulator using a Stewart Platform [Liu et al., 2001].

A variety of actuators have been used, but most common is the piezoelectric stack actuator. An extensive list of novel micro-motion stages using compliant mechanisms is given in Table 2-1. The systems listed are all macro-scale in physical size, with an end-effector that can provide micro-scale motion. There is also a class of micro-scale mobile robots that provide micro-motion, but these are not discussed in this literature review. In addition to the novel designs given in Table 1 a range of micro-motion stages are available off-the-shelf from a variety of manufacturers, including Physik Instrumente, Piezosystems Jena and Thor Labs.

Designer	Year	DOF	Actuators	Compliant mechanism details	Application
Scire and Teague	1978	1	Piezoelectric stack	Planar monolithic using flexure hinges	Electron microscope probe
Smith et al.	1987	1	Electro-magnetic	Planar monolithic using flexure hinges	Micropositioning
Han et al.	1989	6	Rotary motors	Stewart Platform with flexure hinges	To increase accuracy of macro-scale robot
Okazaki	1990	1	Piezoelectric stack	Planar monolithic using flexure hinges	Diamond turning machining
Fukuda et al.	1991	6	Piezoelectric stack	Serial stacked arrangement of piezo fitted to flexible joining members	Micromanipulation
Tomita et al.	1992	6	Piezoelectric stack	Spatial mechanism using flexure hinge	Micropositioning
Arai et al.	1993	6	Piezoelectric stack	Stewart Platform with flexure hinges	Micromanipulation
Morishita et al.	1993	3	Piezoelectric stack	Combination of 1-DOF stages using flexure beams	Micromanipulation

Furukawa et al.	1995	1	Piezoelectric stack	Planar monolithic using flexure hinges	Scanning devices
Kusakari and Yoshikawa	1996	3	Piezoelectric stack	Spatial monolithic using flexure hinges	Micropositioning
Yang et al.	1996	1	Piezoelectric stack	Planar monolithic using flexure hinges	Micropositioning
Chang and Kim	1997	3	Piezoelectric stack	Planar monolithic using flexure hinges	Wafer positioning
Goldfarb and Speich	1997	3	Voice coil	Unique split-tube flexures	Micromanipulation
Lee and Kim	1997	3	Piezoelectric stack	Planar monolithic using flexure hinges	Lithography
Ojala	1997	7	Piezoelectric stack	Stewart platform using flexure hinges	Micromanipulation
Ryu et al.	1997	3 & 6	Piezoelectric stack	2 stage 3-DOF planar monolithic and 3-DOF spatial, using flexure hinges	Wafer positioning
Wang et al.	1997	6	Piezoelectric stack	2 stage 3RRR planar monolithic and 3-DOF spatial, using flexure hinges	Micromanipulation
Chang and Du	1998	1	Piezoelectric stack	Planar monolithic using flexure hinges	Micropositioning
Kallio et al.	1998	3	Piezoelectric Bimorph	Spatial flexure	Micromanipulation
Chang et al.	1999	3	Piezoelectric stack	2 stage planar monolithic using flexure hinges	Lithography
Ohya et al.	1999	3	Piezoelectric stack	Stewart platform using flexure hinges	Micromanipulation
Gao et al.	1999	2	Piezoelectric stack	Planar monolithic using flexure hinges	Micropositioning
Gao et al.	1999	6	Piezoelectric stack	2 stacked mechanisms using flexure hinges	Micropositioning
Gao et al.	2000	1	Piezoelectric stack	Planar monolithic using flexure hinges	Stepping positioner
Hesselbach et al.	2000	3	Piezoelectric slip-stick	Planar using pseudo-elastic flexure hinges	Micromanipulation
Chang and Sun	2001	2	Unique Piezoelectric	Compliance built into actuator	Micropositioning
Chung et al.	2001	3	Piezoelectric stack	Spatial using flexure hinges	Micromanipulation
Elmustafa and Lagally	2001	1	Piezoelectric stack	Planar monolithic using flexure hinges	CNC milling tool control
Yi et al.	2002	3	Piezoelectric stack	3RRR monolithic using flexure hinges	Micropositioning
Woronko et al.	2003	1	Piezoelectric stack	Planar monolithic using flexure hinges	CNC lathe tool control
Yu et al.	2003	3	Piezoelectric stack	Spatial mechanism using flexure hinges	Micromanipulation
Culpepper et al.	2004	6	Electro-magnetic	Planar monolithic	Nanomanipulation

Table 2-1 – Novel Micro-Motion Stage Designs.

The majority of stages mentioned use compliant mechanisms with parallel structures, which have closed loop kinematic chains. Parallel structures provide high rigidity; high accuracy motion; light link mass, as the actuators are located in the base; and high resonant frequency. These advantages make them more suited to high accuracy applications than serial structures.

The stages listed in Table 1 provide a variety of movement ranges and resolutions. The resolution and accuracy of the motion generally depends on the capability of the actuator used and on the type of sensor used to measure the motion. Sensing methods such as strain gauge, capacitive, hall-effect, LVDT, eddy-current, laser interferometer and visual feedback using a microscope have all been used. The sensors can be used to provide feedback for closed loop control or for calibration of open loop control. Both these options have been commonly applied. However, micro-motion stage control will not be discussed at any length in this review.

2.2 Advantages of the 3RRR compliant mechanism

The 3RRR mechanism has a number of advantages that encourage its application in micro-motion stages.

Due to its symmetry it is relatively insensitive to thermal expansion errors, which would adversely affect the kinematics of the mechanism. This advantage is particularly beneficial for very high precision stages and has been an incentive for numerous researchers to develop micro-motion stages using a variety of symmetric compliant mechanisms including the 3RRR topology [Ryu, 1997], [Hesselbach et al., 1998], [Yi, 2002] and [Culpepper et al, 2004].

It has also been found that the 3RRR compliant mechanism can be designed to have decoupled stiffness between the actuators [Handley, 2002]. This is a useful characteristic as it improves the control of the stage as motions from one actuator do not cause disturbance of the other actuators. The controller design is simplified as each actuator behaves independently from the others and therefore three independent linear single-input-single-output (SISO) controllers can be used. The advantages of decoupled mechanism design have been previously exploited in the design of different topology micro-motion stages by specifically designing the compliant mechanism to reduce coupling. Using this approach other researchers have been able to reduce actuator coupling of their micro-motion stages to less than 5% [Tomita et al. 1992] and 3% [Lee and Kim, 1997]. Decoupled mechanism design has not previously been applied to a 3RRR compliant mechanism, however coupling in a 3RRR compliant mechanism has been noted to be less than 0.3% [Handley, 2002a, 2002b]. To achieve decoupled design, a macro-scale 3RRR mechanism has been studied in a remote-centre of compliance (RCC) device to be used in assembly operations [Kim 1997, 2000]. It has been observed that, when the 3RRR mechanism has symmetrical linkages and stiffness, and is in its central position, the compliance matrix is decoupled. This means that when an external force or torque is applied it will deflect only in the direction of the applied force/torque.

The 3RRR compliant mechanism can also provide amplified $XY\theta_Z$ motion using a single compliant mechanism with a simple and lightweight structure. This minimises the number of actuators required and allows relatively large output motion to be achieved using small actuators. This can allow a compact design with small overall

size. In addition the lightweight structure could potentially have a higher natural frequency than more complex and heavier designs. This can increase the overall system bandwidth. Other systems providing $XY\theta_z$ motion have been developed that use an X-Y stage with a separate rotation stage mounted on top, but this creates a relatively heavy and bulky stage, which may require more than three piezo-actuators. An example of such a stage is given in Figure 2-4 [Chang et al. 1999]. This stage uses six piezo-actuators, does not significantly amplify the input motion and has dimensions of 200x200x50mm, although this design does have low crosstalk interference, with coupling between degrees-of-freedom of less than 1%.

NOTE: This figure is included on page 18 of the print copy of the thesis held in the University of Adelaide Library.

Figure 2-4 – Schematic of a two-part $XY\theta_z$ micro-motion stage (a) x-y translation stage, (b) rotation stage [Chang et al., 1999].

Other stages that provide $XY\theta_z$ motion with a single monolithic planar compliant mechanism have been developed. An example is given in Figure 2-5 [Lee and Kim, 1997]. This stage does not amplify the piezo-actuator displacement and is therefore relatively bulky for the output motion achieved and it also introduces some coupling between the actuators.

NOTE: This figure is included on page 19 of the print copy of the thesis held in the University of Adelaide Library.

Figure 2-5 - Schematic of a $XY\theta_z$ micro-motion stage using a single monolithic compliant mechanism [Lee and Kim, 1997].

2.2.1 Micro-motion stages using the 3RRR compliant mechanism

Two of the micro-motion stages listed in Table 1 [Wang, 1997] and [Yi, 2002] use the 3RRR compliant mechanism. Another stage [Ryu, 1997] uses a very similar topology compliant mechanism. Another stage with similar topology has been developed by [Hesselbach et al., 2000]. However, this uses notch flexure hinges made from shape memory alloy (SMA), which provides the stage with significantly different behaviour to flexure hinges made of conventional metals. It will therefore be considered to be in a different class of stage and not discussed in detail in this review.

The 3RRR topology compliant mechanism using circular profile flexure hinges was proposed [Wang, 1997] as part of a two-stage design that would provide 6-DOF, as shown in Figure 2-6. The 3RRR stage would provide 3 planar degrees-of-freedom,

while mounted to this would be another stage to provide 3 more degrees-of-freedom. The design concept and kinematic and dynamic modelling was presented, but a prototype was not constructed and tested.

NOTE: This figure is included on page 20 of the print copy of the thesis held in the University of Adelaide Library.

Figure 2-6 - DOF micro-motion stage design using the 3RRR compliant mechanism presented by Wang et al. (1997).

Later work [Zou, 2000], [Zhang, 2002] presented further investigation of the 3RRR compliant mechanism. The kinematic model was discussed in detail and a prototype was presented along with experimental results. The 3RRR compliant mechanism was wire-cut from a single piece of material, as shown in Figure 2-7; three stack piezoactuators were assembled into this; and the end-effector was bolted on top. The work presented in this thesis is a continuation of this previous work. A second prototype $XY\theta_Z$ micro-motion stage using this 3RRR compliant mechanism has been presented in [Lu, Handley and Yong, 2004].

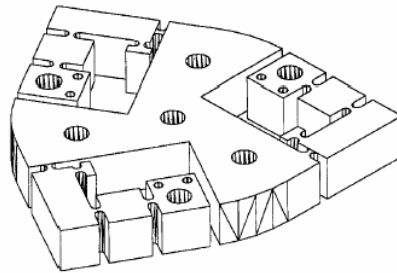


Figure 2-7 - 3RRR compliant mechanism presented by Zou (2000) and Zhang et al. (2002).

A topology of compliant mechanism similar to the 3RRR has also been presented [Ryu, 1997 (a),(b)] as shown in Figure 2-8. The compliant mechanism using circular flexure hinges and end-effector was wire cut from a single piece of material. The mechanism consists of three linkages, which are each a double compound lever with six flexure hinges, attached to the central end-effector. Each linkage was driven by a stack piezo-actuator. A unique modelling method was presented to model the compliant mechanism and an optimal design approach used to design the mechanism to give maximum rotation. A prototype was then manufactured and tested.

NOTE: This figure is included on page 22 of the print copy of the thesis held in the University of Adelaide Library.

Figure 2-8 - Planar 3-DOF compliant mechanism presented by Ryu et al. (1997).

A different configuration of 3RRR compliant mechanism was presented [Yi, 2002] as shown in Figure 2-9. This design also uses circular flexure hinges. The compliant mechanism and end-effector were wire cut from a single piece of material. This design incorporates some flexure hinges that were designed to be compliant axially as well as in rotation, so that these hinges provide 2-DOF. This gives the mechanism mobility of six instead of three and therefore six piezo-actuators are needed to control the end-effector. The kinematic and stiffness modelling of the compliant mechanism was presented and a prototype was constructed and tested.

NOTE: This figure is included on page 23 of the print copy of the thesis held in the University of Adelaide Library.

Figure 2-9 - 3RRR compliant mechanism presented by Yi et al. (2000).

2.3 Micro-motion stage modelling

To aid in the design of micro-motion stages kinematic and dynamic models are needed. The kinematic model gives the relationship between actuator input displacements and end-effector output displacement. All motion stages require a kinematic model in order to control the end-effector position. In the majority of cases a kinematic model has been developed at the design phase so that an appropriate mechanism may be designed. The dynamic model gives the relationship between input forces and the resulting acceleration, velocity and displacement of the stage. Dynamic models have been derived less frequently.

The micro-motion stages considered in this review consist of flexure hinge based compliant mechanisms and actuators such as piezo-actuators. Most discussion of micro-motion stage modelling presented in the literature has considered only the modelling of the compliant mechanism. The piezo-actuator has been considered independently and numerous models have been developed. However the piezoactuator model has rarely been integrated into the compliant mechanism model to

give a total micro-motion stage model. A few studies have included the piezo-actuator to give a total micro-motion stage model and these will be discussed separately.

2.3.1 Compliant mechanism modelling

As systems using compliant mechanisms have been developed new methodologies have been developed to model them. While exhaustive research has been conducted over the years into the area of rigid body mechanics, compliant body mechanics is less well understood. Compliant mechanisms differ to rigid body mechanisms in that they possess at least one compliant element whose deformation allows the displacement of the mechanism. Compliant mechanisms can possess a variety of compliant elements. Notch flexure hinges, as shown in Figure 2-1, are elements that deform through a short segment and therefore behave like a revolute joint. Compliant beam elements deform along their entire length, while more complex distributed-compliance structures are flexible throughout the entire mechanism. Notch flexure hinges are commonly used in micro-motion stages as they provide predictable motion and are relatively rigid. The micro-motion stage studied in this thesis uses notch flexure hinges to derive its motion and therefore this literature review will focus on modelling methods for compliant mechanisms using notch flexure hinges.

At this point it may be helpful to clarify that compliance is the inverse of stiffness.

2.3.1.1 Notch flexure hinge modelling

Many compliant mechanisms derive their compliance using notch flexure hinges, as shown in Figure 2-1. This hinge is designed to provide rotational compliance about one axis only, however some compliance in other axes is unavoidable. The hinge parameters affect the amount of compliance in all axes and also the range of motion of the hinge in the axis of rotation. Therefore it is important to have an accurate means to model the hinge and select suitable hinge parameters.

This review will only consider the modelling of hinges using materials with linear elastic behaviour. In recent research notch flexure hinges have been developed and modelled that use shape memory alloy (SMA), which has pseudo-elastic behaviour [Hesselbach et al., 2000]. This provides up to 15% elastic strain, compared to conventional metallic materials with approximately 0.4% elastic strain.

The notch flexure hinge can have a variety of profiles; circular, rectangular, corner filleted, elliptic, parabolic or hyperbolic. In early designs notches were machined by drilling two closely spaced holes to give a circular notch, or by clamping a thin leaf to give a rectangular profile "leaf-spring". Therefore circular and rectangular profiles have been widely used and studied. In recent years the common use of wire electro-discharge machining (EDM) has made it possible to select other hinge profiles such as elliptical, parabolic, hyperbolic and corner filleted.

The circular cross section flexure hinge was first thoroughly investigated by Paros and Weisbord (1965). They developed both exact and simplified analytical

formulations to determine the hinge stiffness about all three axes. The equations they presented were actually for a rectangular single-axis hinge but were claimed to be applicable to a circular single-axis hinge with little loss in accuracy. In their work they did not present finite-element-analysis (FEA) or experimental validation of the formulations. Nonetheless their formulations have been widely applied in the design of subsequent compliant mechanisms.

More recently a number of researchers have used FEA to model flexure hinge designs with more accuracy. Smith et al. (1987) used circular notch flexure hinges in the design of a compound linear spring and used FEA to determine the bending stiffness of the hinge about the Z-axis only. They did not experimentally verify the accuracy of their model or make any reference to the work of Paros and Weisbord.

Her and Chang (1994) also used FEA to determine the bending stiffness of the circular flexure hinges used in their stage design and they presented a design chart of stiffness for various choices of hinge radius, R , and thickness, t . Their FEA predicted stiffness was significantly different to that derived using the analytical equations of Paros and Weisbord, particularly for high R/t ratios, but these results were not experimentally verified.

Rong et al. (1994) derived compliance equations for the circular flexure hinge, resulting in equations that could be reduced to the Paros-Weisbord equations. Using the simplified Paros-Weisbord equations they derived compliance ratios, which relate the compliance in the desired motion axis to compliance in the other undesired

motion axes. Ideally, compliance should be high in the motion axis and low in the other axes, so that the motion accuracy will be high. No comparison was made between theoretical and experimental results.

Xu and King (1995, 1996) used FEA to consider the compliance, accuracy and maximum stress of different flexure hinge topologies in bending about the Z-axis. They investigated elliptic and corner filleted topologies and compared these with the traditional circular flexure hinge. This work found that the circular profile provides the most accurate motion, making it particularly suited to precision motion applications, but it is also the least flexible which limits the motion range of the hinge. They suggested that for precision-motion applications requiring less than 0.1mm of displacement and a small output force the circular hinge was appropriate. Furthermore they found that compared to the corner filleted hinge the elliptical hinge is less flexible but more accurate. The general trend for both hinges is that high accuracy is coupled to less compliance. Their study of the hinge maximum stress revealed that the elliptic hinge was able to achieve greater compliance with relatively lower maximum stress, regardless of the load force, compared to both the corner fillet and circular hinges. This was because the corner fillet produces a major stress concentration in the corner, while the circular hinge produces the maximum stress in the centre of the web, which is the thinnest section. To verify the FEA they built a simple lever amplifier for one topology of flexure hinge. The difference between the experimental lever output and the FEA model output was less than 10%.

Xu and Qu (1996) studied the circular flexure hinge and used FEA to derive design charts giving the relationship between rotational stiffness only and various hinge parameters. They also considered the effect of machining errors. They did not present a comparison of their predicted stiffness to that predicted by other researchers or experimentally verify their results. Inspection of their results demonstrates that the stiffness predicted by their model differed significantly to the prediction of Paros and Weisbord.

Smith et al. (1997) investigated flexure hinges with an elliptic profile and presented closed form equations for compliance based on a modification of the Paros-Weisbord equations. The right circular hinge was studied as a limiting case of the elliptic profile for which the equations converged to those of Paros-Weisbord. They considered a variety of hinge geometries, including three right circular hinges with $t/2R = 0.06, 0.12$ and 0.2 , and compared the bending stiffness predicted by the analytical equations with FEA. The FEA result for the circular hinges was shown to be within 11% of the analytical equations, which was the worst case when compared to the elliptical profiles. They then experimentally verified the models and demonstrated that the analytical equations were within 10% of the experimental, which again was the worst case compared to the elliptic profiles. Based on the FEA they also presented stress concentration factors for the hinges.

Zhang and Fasse (2001) also modelled the circular hinge using FEA. They generated approximate functions to relate rotational hinge compliance to hinge dimensions and material parameters. They compared their results to Paros-Weisbord, Smith et al. and

Braak which demonstrated that their results differ to the analytical equations, but they did not present experimental verification to support their result.

More recently researchers have developed new analytical formulations to model flexure hinges. Tseytlin (2002) presented new tractable equations for rotational stiffness only of the circular hinge and presented a comprehensive comparison between the analytical, FEA and experimental stiffness determined by various researchers. This work indicated that the new analytical equation gave a better prediction than those of Paros and Weisbord.

Wu and Zhou (2002) also developed new and convenient equations to determine the stiffness of circular flexure hinges about all 3 axes. Their equations gave the same stiffness prediction as the exact Paros and Weisbord equations. They also compared the exact equation that they had derived with the simplified equations of Paros and Weisbord and demonstrated that the simplified equation gives considerable error as the hinge thickness approaches the hinge radius. They did not experimentally verify their results.

Lobontiu et al. (2002 (a)) presented closed form equations for elliptic, parabolic, hyperbolic and circular profile hinges. They considered only in-plane compliance and demonstrated that the circular equations were equivalent to Paros-Weisbord. FEA was used to verify the analytical equations within 10% error. They compared the compliance and precision of rotation of all the different hinge profiles. This revealed that the circular hinge has the most precise rotation but also the least

compliance compared to the others. In a second paper Lobontiu et al. (2002(b)) again presented closed form equations for parabolic and hyperbolic hinge profiles and this time considered in plane and out-of-plane compliances. They also evaluated stress levels in terms of compliances. FEA and experiment was used to verify the analytical equations. The FEA and analytical equations were within 8%. One sample of each hinge type was fabricated and tested and this was within 4% of the analytic result. Comparing the parabolic and hyperbolic profiles it was concluded that the parabolic hinge was more compliant about the input axis and subjected to less stress, whereas the hyperbolic flexure was less sensitive to parasitic loading effects. In this paper no comparison was given to the circular profile.

Lobontiu (2002 (c)) presented a finite element modelling method for single axis flexure hinges that used just 3 nodes to represent the flexure hinge. The elemental stiffness and mass matrices were presented in a generic integral form that enables specific solutions to be found for different hinge shapes. A 2-node line element was then presented to model quasi-rigid links. A corner-filletted hinge and link were modelled using this simplified FEA method and compared to a full mesh FEA. The error of the simple FEA was less than 6%.

Schotborough (2004) presented dimensionless design graphs for three types of flexure elements, including the circular notch flexure hinge. These graphs were derived using FEA and could be used to help a designer select appropriate hinge parameters to provide the desired stiffness and rotation for the flexure hinge. The results of this work were not compared to analytical equations or experimentally verified.

Ryu (1997 (c)) also studied the right circular flexure hinge and investigated induced motion errors caused by various types of machining error. The 6x6 stiffness matrix they formulated to model the flexure hinge in all axes used the Paros-Weisbord equations to determine the value of the stiffness elements. Therefore the accuracy of this model is limited by the accuracy of those equations. They presented a simulation of a simple compound linear spring that demonstrated that machining errors could have a serious effect on the in-plane and out-of-plane motion error. However, the type of machining process used determines the extent of the machining error and thus motion error. Drilling and reaming processes can introduce significant error, whereas EDM fabrication does not introduce significant error.

The results presented in the literature [Xu and King, 1995,1996] , [Lobontiu, 2002] suggest that the circular hinge profile gives the most precise rotation. Therefore for applications requiring precision and predictable motion the circular hinge profile is most appropriate. The design of the 3RRR compliant mechanism will therefore use only the circular profile flexure hinge. The majority of analytical stiffness equations presented concur with the exact equations of Paros-Weisbord and therefore any of these equations may be used in modelling without significant difference. The FEA comparisons presented suggest that the accuracy of the analytical equations varies depending on the hinge parameters. However, without experimental verification it is impossible to know if the FEA or analytical equations are more accurate. Experimental verification has only been presented for a limited number of hinge parameters, but the results suggest that the equations are within 10% of experiment. This suggests that the analytical equations give a useful prediction of stiffness.

2.3.1.2 Compliant mechanism modelling

The notch flexure hinge, as shown in Figure 2-10(a), is designed to predominantly provide rotation about one axis only. Therefore the simplest technique to model a compliant mechanism is to model flexure hinges as 1-DOF purely revolute joints with torsional stiffness, joined by rigid links, as shown in Figure 2-10(b).

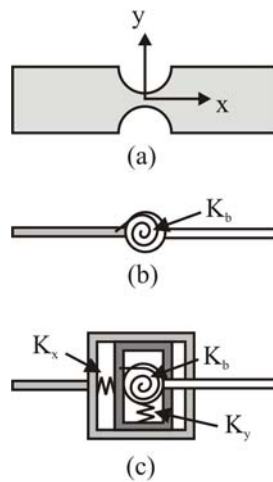


Figure 2-10 - (a) Schematic of flexure hinge, (b) 1-DOF model, (c) 3-DOF model

In this way compliant mechanisms can be modelled using well-understood rigid-body equations and kinematic and dynamic models can be derived using standard robotics analysis. Such a model has been termed a pseudo-rigid-body model (PRBM). This simple modelling method has been demonstrated to be effective, and much work has been conducted in the last decade to formalise a design approach. Howel and Midha (1994, 1996), and Salmon et al. (1996) have been the major proponents of this work. They have considered flexure hinge mechanisms as a simple case but have focused most attention on distributed compliance mechanisms, both

macro and micro scale. The PRBM is the most commonly used method to model compliant mechanisms using flexure hinges.

However, flexure hinges do not provide purely revolute motion. The flexure hinge also has compliance in other degrees of freedom, as shown in Figure 2-10(c) for in-plane compliances only, and therefore motions in these other DOF will usually be observed. The extent of these other motions depends on the design of the compliant mechanism. Some designs of compliant mechanism are such that the mechanism will be over constrained and axial compliance of the hinge is necessary to provide motion. In these cases especially the accuracy of the PRBM is limited. In some cases the simple PRBM has been improved by considering translational compliances in the flexure hinges. This means that the hinge has more than 1-DOF and the model becomes more complicated.

The most accurate modelling method is based on finite-element-analysis (FEA). However this approach is also the most computationally demanding and requires special software, such as ANSYS. In the design of micro-motion stages it is common for more than one approach to be applied. The PRBM is commonly used to give an initial prediction. If this does not give an accurate enough result then another more accurate, but complex, method may be applied.

The earliest application of the PRBM type approach was presented by Scire and Teague (1978) in the design of their 1-DOF micropositioning stage. Their stage and model are shown in Figure 2-2. Their analysis aimed to model the kinematic

behaviour of the stage and predict the output displacement of the amplifying linkage. The PRBM alone did not give very accurate results as the design of their stage was over-constrained. The meaning of this can be better understood by inspection of Figure 2.2. If the joints were to be purely revolute, and the links purely rigid, then any motion of the links would not be possible, as the end-points of the rotating links need to move away from each other. To provide motion requires axial deformation of some hinges, which the PRBM cannot predict. This situation is found in several other compliant mechanism designs, which will be discussed in this review. Scire and Teague further improved their analysis by also considering the axial strain in the most stressed flexures. They applied the analytical equations developed by Paros and Weisbord to model the flexure hinges and select suitable hinge parameters. As this theoretical analysis proved to be sufficiently accurate design tool they did not develop a general modelling method.

Han et al. [1989, 1990] presented the modelling of a 6-DOF micromanipulator using a Stewart Platform. They analysed the manipulator using analytical kinematic and dynamic models based on a PRBM approach and used the kinematic influence coefficient and virtual work principle. They also presented FEA of the flexure hinge and leg. The models were not experimentally verified.

Tomita et al. (1992) designed a 6-DOF ultra-precision stage that used a parallel compliant mechanism and six piezo-actuators. The kinematic model of this design was simple as there were no displacement amplifying linkages. They modelled this as a mass-spring system and derived the dynamics using the Lagrangian method.

Pseudo-rigid-body model assumptions were made and no attention was paid to axial deformation of the flexure hinges. The analytical predictions of static behaviour were close to the experimental results, while the prediction of natural frequency deviated from the experimental result by approximately 25%.

In the case of micro-motion stages the displacement of the mechanism is very small and thus it is possible to make some simplifying approximations in the modelling. This has lead researchers to develop new modelling approaches specific to micro-motion compliant mechanisms. Her and Chang (1994) developed a linear scheme for the displacement analysis of a flexure hinge micro-motion stages. The PRBM approach was applied, but furthermore the scheme linearised the geometric constraint equations and made small displacement angle approximations. They also presented an FEA calculation of flexure hinge stiffness. They considered a single closed-loop linkage and compared the kinematic behaviour predicted by the linear scheme, to that predicted by a FEA model. Both models predicted similar behaviour. This modelling method can be also applied to stages with multiple loops. Her and Chang also considered the case where the mechanism is over-constrained, such as the stage developed by Scire and Teague. They stated that in this case a link must deform, however it is much more realistic that, in this case, the flexure hinge will axially deform. Such deformation is not modelled by a standard PRBM. They compared Scire and Teague's PRBM analysis, the linear scheme and a FEA model. The linear scheme predicted kinematic behaviour much closer to the FEA result than the PRBM. This linear scheme provides a general modelling method for planar

mechanisms that is more accurate than a PRBM and far more computationally efficient than the FEA. Her and Chang did not experimentally verify their results.

Rong et al. (1994), as mentioned in the previous section, considered the circular flexure hinge and derived compliance ratios, which related the compliance in the desired motion axis to compliance in the other (undesired) motion axes. In addition to this they investigated the design of a 1-DOF linear guiding mechanism and made some simple recommendations based upon a PRBM analysis. The mechanism they designed was over-constrained and axial elongations of the flexure hinges were to be expected, but this was not modelled or discussed. A kinematic model was not derived and no comparison was made between theoretical and experimental results.

Gao et al. (1999) developed two different planar micropositioning mechanisms utilising circular flexure hinges and piezo-actuator. Their 2-DOF mechanism consists of two similar 1-DOF stages orthogonally mounted in a serial arrangement. They presented a static and dynamic analysis of the stage. Their static analysis was similar to the approach of Scire and Teague and, as the end-effector was over-constrained, they needed to include the axial elongation of the flexure hinges in their static model. They used the simplified Paros-Weisbord equations to determine the rotational and axial compliance of the hinges. A linear dynamic model was then derived using the Lagrangian method, neglecting the link mass, and an equation for the natural frequency was derived. The dynamic model they presented consists of only inertia and stiffness terms. It was presumably assumed that damping, Coriolis/centripetal or gravity terms were insignificant. They claimed to use the model to select parameters

to give optimal natural frequency and motion range, although no details of the optimisation method were given. They presented experimental results that demonstrated that the natural frequency of one 1-DOF mechanism was 558Hz compared to 575Hz predicted by the model. They did not compare the analytical model displacement to the experimental displacement. Gao et al. (1999) also developed a 6-DOF micropositioning stage. This used a 3-RPR (revolute-prismatic-revolute) stage to provide 3 planar DOF. The forward and inverse kinematics was derived for the micropositioner based upon a PRBM and using small displacement angle approximations. This resulted in a constant Jacobian to represent the kinematics. The derivation did not consider axial deformation of the flexure hinges and they did not consider a static analysis. They also did not experimentally verify their model so the accuracy of this method was not demonstrated.

Ohya et al. (1999) developed a spatial 3-DOF micromanipulator using circular notch flexure hinges and spherical joint flexure hinges, driven by piezo-actuators. The kinematic model was derived for this using a standard robotics approach based upon a PRBM. No mention was made of axial deformations of the hinges. The accuracy of the model was not experimentally verified and the kinematic model was not used in control. Instead a constant Jacobian matrix was experimentally derived during a calibration process and this was used in control.

Chung et al. (2001) investigated a 3-DOF spatial design micromanipulator and presented a PRBM type analysis to derive the forward and inverse kinematics. The hinge stiffness, calculated using the Paros-Weisbord equations, was used to derive a

stiffness matrix for the mechanism and using this the required actuator torque was selected. The same approach could be used in reverse to select hinge parameters for a given actuator torque. A FEA model was used to derive the forward kinematics which gave similar results to the analytic model. The natural frequency was also calculated using an analytical calculation. A prototype was presented but no comparison was made with the experimental results.

Koseki (2002) applied the matrix method to analyse the kinematic behaviour of a spatial 3-DOF micro-parallel mechanism using circular notch flexure hinges and piezo-actuators. The modelling method they presented had been well developed in architecture to analyse frame structures, but had not previously been applied to flexure hinge mechanisms. This method modelled the compliant behaviour of the flexure hinges in all axes, not only bending. Furthermore the compliance of beam elements was also modelled. It was assumed that the stiffness of members was linear, and that translation and rotations were small enough to be linearised. The method involved establishing a 6x6 compliance matrix for each flexure and beam element in the mechanism and superposition was used to determine the motion of the total structure under an input force. It was therefore a kinetostatic modelling method. It would be expected that this method would give a better prediction of kinematics than a PRBM while being more computationally efficient than a FEA model. A prototype micro-mechanism was manufactured and a calibration experiment conducted. Comparison of the model and experimental Jacobians revealed a significant difference, with Jacobian terms differing by about 50%. The reasons for this difference were not clear.

Lobontiu et al. (2003) presented an analytical method to calculate the displacement and stiffness of compliant mechanisms using flexure hinges. Their method is based on strain energy and uses Castigliano's displacement theorem to produce closed-form equations that incorporate the multi-DOF compliance characteristics of the flexure hinges, along with the other geometric and material properties of the compliant mechanism. This method can be applied to calculate displacement and stiffness of any serial compliant mechanism and was demonstrated by application to a 1-DOF amplifying mechanism. This is a lower cost alternative to FEA. FEA was used to confirm the analytical predictions, with less than 5% error in the predicted displacement amplification and stiffness, but there was no experimental verification. They also presented the displacement amplification predicted by a PRBM for a range of mechanism geometries. The PRBM overestimated the amplification of the mechanism by between 70 and 300%. In this work the method was not applied to a parallel multi-DOF mechanism and it was not clear how applicable the method would be to this class of mechanism.

Yu et al. (2004) designed a parallel spatial 3-DOF micromanipulator that uses a compliant mechanism based upon the modified Delta mechanism and is actuated by piezo-actuators. They modelled this using a PRBM and derived a constant Jacobian to describe the kinematics. They conducted experiments that revealed error in theoretical kinematics, in particular there was unexpected rotational motion. To better understand the mechanism behaviour they then analysed its mobility using screw theory and the matrix method. The new analytical results also predicted rotational motion as found in the experiment. However, the authors did not derive a

more accurate kinematic model, nor did they quantitatively demonstrate its accuracy, so it is unclear how valuable this approach is.

Culpepper et al. (2004) presented the 'HexFlex' 6-DOF nanomanipulator. The Hexflex is a novel planar monolithic compliant mechanism using flexure beams that provides 6-DOF motion and uses three 2-axis electromagnetic actuators. The motion of the end-effector is small compared to actuators to improve the resolution of end-effector motion. The design is suited to small-scale or MEMS manufacturing processes and fibre-optic alignment. The symmetrical design makes it insensitive to thermal expansion errors. The HexFlex was modeled using CoMeT™ (Compliant Mechanism Tool) developed by the Precision Systems Design and Manufacturing Research Lab at MIT. CoMeT was written in Matlab and uses beam equations to determine the compliant mechanism stiffness rather than a FEA approach and is therefore faster than FEA. Given user inputs that define the compliant mechanism geometry, material, and constraints, CoMeT develops the global stiffness and compliance matrices via the direct stiffness approach. This modelling method has been verified by experimental results which reveal the model to be within 5% of experimental results.

2.3.1.3 Modelling of the 3RRR Compliant Mechanism

Wang et al. (1997) investigated a 6-DOF micromanipulator that consisted of two stacked 3-DOF stages, using compliant mechanisms and piezo-actuators, as shown in Figure 2-6. The bottom stage was a 3RRR stage similar to that studied in this thesis. They derived the kinematics using vector analysis and PRBM assumptions. Then,

based upon these kinematics, they derived the dynamic model using the Lagrangian method. They did not verify their analytical model with either FEA or an experiment.

Zou (2000) and Zhang et al. (2002) also derived a kinematic model of the planar 3RRR mechanism considered in this thesis. A PRBM was constructed for the 3RRR mechanism and based upon this a constant Jacobian was derived to describe the kinematics. In their approach they first derive a non-linear model and then linearise the kinematics by using a Taylor series expansion as an approximation for the derivation of the displacement variables. This is a valid approach as the displacements of links are sufficiently small. This leads to a constant Jacobian matrix that relates the change of actuator displacement to change of end-effector displacement. Experimental verification was conducted which revealed significant error in the analytical kinematics. This necessitated the use of calibration to improve the kinematic model accuracy.

Other approaches have been used to derive the kinematics of the same 3RRR compliant mechanism studied by Wang, Zou and Zhang. Yong et al. (2004a, 2004b) used the loop closure theory to derive a linear analytical kinematic model of the PRBM of the 3RRR compliant mechanism. Handley et al. (2004a) also used a linear method, based upon the method of Her and Chang (1994), to derive the linear analytical kinematic and dynamic models of the PRBM. The methods of Yong et al. and Handley et al. were similar. Both of the kinematic models derived by Yong et al. and Handley et al. gave the same constant Jacobian matrix as was derived by Zou (2000). However, the method of derivation was computationally simpler.

Ryu et al. (1997 (a),(b)) presented a planar micropositioning stage utilising right circular flexure hinges, driven by 3 piezo-actuators, as shown in Figure 2-8. They presented a model for the mechanism that assumes all the linkages are rigid bodies connected by flexure hinges that are translational/rotational springs and thus the mechanism can be modelled as a mass-spring system. The stiffness of the flexure hinges was calculated using the Paros-Weisbord equations. Each linkage element of the mechanism was considered to be a rigid body with 6-DOF. Stiffness and inertia matrices were then established to describe the kinetostatic and dynamic behaviour of the mechanism. To simplify the analysis only the end-effector mass was included in the model and the linkages were assumed mass-less. The maximum output motion of the mechanism was then calculated assuming that the piezo-actuator would provide the same displacement as in the unloaded case. The model was used to determine an optimal design to provide maximum rotation. A prototype was fabricated and experiments were conducted to validate the model. The actual output motion and natural frequency were significantly less than predicted by the model. The error in output motion was suggested to be due to the real piezo-actuator displacement under load being less than the maximum unloaded displacement. Later experiments by Ryu et al. (1999) gave a detailed comparison of the real vs. the model displacement input/output behaviour of the compliant mechanism. This showed that the model prediction was close to the experimental result, but calibration was required so that the model could be used for open-loop control within 5% error. Furthermore, it is useful to note that this particular mechanism has an over constrained linkage and therefore axial deformation of the flexure hinges was expected to provide motion. They did not present a PRBM or FEA for comparison with their results.

Yi et al. (2002) investigated the modelling of a 3RRR compliant mechanism, as shown in Figure 2-9, and discussed the modelling of flexure hinges. They discussed the inaccuracy introduced by considering flexure hinges to have only 1-DOF and proposed that a 2-DOF model considering the flexure hinge to be both a revolute joint and prismatic joint could be used to increase accuracy. They also discussed the mobility of the mechanism that resulted when the flexure hinges have more than 1-DOF. If all joints were to have 2-DOF then the mobility would be 12, but this would require 12 actuators to control. As a compromise they presented a 3RRR mechanism with mobility 6, that uses 3 joints designed to have 2-DOF, and can be controlled using 6 piezo-actuators. The kinematic and stiffness models were derived for both the mobility 3 and mobility 6 compliant mechanisms. The links were assumed to be rigid. An FEA model was then created for comparison with the analytical results. It was found that the mobility 3 analytical model had significant error while the mobility 6 model was close to the FEA. Experiments were also conducted to determine the stiffness of the mobility 6 mechanism. The analytical stiffness error was approximately 30%. This was an interesting approach but it seems impractical to introduce extra complications and expense by increasing mobility and the number of actuators. Furthermore the mechanism still has six joints which are modelled as 1-DOF which would introduce errors due to their unmodelled compliance.

None of the 3RRR compliant mechanism models presented so far has incorporated piezo-actuator modelling into the compliant mechanism model to give a total micro-motion stage model.

2.3.1.4 Workspace of the 3RRR compliant mechanism

Given the kinematic model of a 3RRR compliant mechanism it is possible to investigate the workspace area of the 3RRR compliant mechanism. Handley et al. (2004b) presented a study that identified the shape, size and possible orientations of the workspace of a 3RRR compliant mechanism. However, this study was based upon a PRBM of the compliant mechanism, whose accuracy had not been demonstrated, and was performed for only one particular configuration of mechanism.

2.3.2 Piezo-actuator models

The displacement of piezo-actuators is commonly controlled using a voltage input. When a voltage input is used the piezo-actuator displays a non-linear displacement response with hysteresis as shown in Figure 2-11. The piezo-actuator also experiences drift.

NOTE: This figure is included on page 44 of the print copy of the thesis held in the University of Adelaide Library.

Figure 2-11 - Voltage vs. generated displacement characteristics for a stack piezo-actuator [Tonkin, 2000].

The dynamic modelling of a piezo-actuator including its non-linear behaviour is not straight forward, but numerous models have been derived. Purely parametric models have been derived [Ge and Jouaneh,1995], [Goldfarb and Celanovic, 1997], [Adriaens et al, 2000]. Other models have used a parametric Preisach hysteresis model in conjunction with experimentally determined dynamic linear model [Zhou et al, 1999]. While various experimentally determined piezo-actuator models have also been presented [Croft and Devasia, 1997,1998, 2001]. However, the non-linear behaviour of the piezo-actuator can be compensated for by the use of closed loop control, while this behaviour has only little effect on the overall stage performance. Therefore, non-linear modelling of the piezo-actuator will not be considered in this thesis.

A commonly used linear dynamic model for the piezo-actuator [Goldfarb and Celanovic, 1997] is given in Figure 2-12.

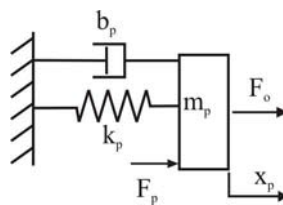


Figure 2-12 - Linear dynamic model of a piezo-actuator.

In this figure k_p , b_p , m_p are the stiffness, damping and mass of the piezo-actuator ceramic, respectively, F_p is an internal force which is proportional to the applied voltage and F_o and x_p are the output force and displacement, respectively, generated by the actuator. The piezo-actuator characteristics that most affect the micro-motion

stage performance are the actuator displacement, force generation and stiffness. Therefore, a linear quasi-static model that considers only x_p , F_o and k_p , as shown in Figure 2-13 (top), may be sufficient for integration into a micro-motion stage model [Goldfarb and Celanovic, 1999]. The operating area of a piezo-actuator is given approximately by Figure 2-13 (bottom).

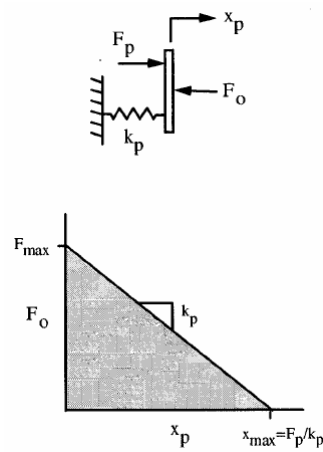


Figure 2-13 - (top) Quasi-static model of stack piezo-actuator and (bottom) region of operation.

When integrated into a compliant mechanism with stiffness, $k_{mechanism}$, the piezo-actuator experiences a spring load that will reduce its displacement. Eqn (2.1) [Physik Instrumente, 2006] can be used to approximately determine the displacement of the loaded piezo-actuator, x_{load} , given its displacement when no load is applied, $x_{no-load}$, and its stiffness, k_p .

$$x_{load} = x_{no-load} \left(\frac{k_p}{k_p + k_{mechanism}} \right) \quad (2.1)$$

This effect on piezo-actuator displacement may also be useful within a micro-motion stage model.

2.3.3 Micro-motion stage models incorporating compliant mechanism and piezo-actuator

Furukawa et al. (1995) presented a kinematic and dynamic analysis of a 1-DOF compliant amplification mechanism using circular flexure hinges. They first determined the amplification of the mechanism using a PRBM approach and then incorporated the effect of axial compliance of the hinges. They used the Paros-Weisbord equations to calculate the hinge compliance in bending and axial stretching. One component with complex shape was analysed using FEA to determine its stiffness. They also derived a static design equation for the maximum output displacement of the stage that included the effect of the compliant mechanism stiffness on the piezo-actuator displacement. It was observed that the stiffer the mechanism the less the piezo-actuator displacement. The equation they used for the relationship between output force (F) and output displacement (Y) of the piezoelectric stack at the maximum applied voltage is given in Eqn (2.2),

$$F = -\left(\frac{F_o}{Y_o}\right)Y + F_o \quad (2.2)$$

where F_o and Y_o are the blocked force and no-load output displacement of the piezo-actuator, respectively.

They then also derived the natural frequency of the stage and presented a graph of output displacement and natural frequency vs. the thickness of the flexure hinges, t . This result proved useful during the design stage, where a compromise needs to be found between natural frequency and output displacement of the stage. Increasing the mechanism stiffness will increase the natural frequency, but increased mechanism stiffness will increase the load on the piezo-actuator and reduce its displacement. They experimentally verified their result and found that the predicted amplification was in close agreement with the experiment, while the natural frequency prediction was within 20% of the experiment.

Yang et al. (1996) also investigated the design of a 1-DOF micropositioning stage with a compliant mechanism using circular flexure hinges and actuated by a piezo-actuator. They first derived analytical equations for static and dynamic analysis of the stage based on a PRBM type analysis and used the Paros-Weisbord equations to calculate the bending stiffness of the hinges. This model also included a static term to predict the piezo-actuator displacement under a spring load. This initial analysis did not consider axial deformation of the hinges. A FEA model was then created to evaluate the analytical model. The error in displacement prediction between analytical model and FEA was 30%. The design of this mechanism was over-constrained, requiring elongation of the flexure hinges. Therefore, an improved analytical stiffness model was derived that included axial compliances of the hinges. The error in displacement prediction between the improved model and the FEA was now only 2%. The derivation of the analytical dynamic model was based on a PRBM type analysis in combination with the Lagrangian method. The piezo-actuator was

included as a stiffness term. An improved dynamic model was also presented that used an FEA software package to model the flexure hinges as joints with 3-DOF; x-, y- translation and z-rotation, joined by rigid links. The stiffness of the hinges was determined using an FEA of the flexure hinge. The difference between the models was less than 3%. The results were experimentally verified and the experimental output displacement was only 10% higher than predicted by the analytical model. The stiffness predicted by the FEA was within 5% of the experiment value, while the FEA natural frequency was within 4% of the experiment.

Further work by Jouaneh et al. (2003) developed a general approach for the design of lever mechanisms using circular flexure hinges. They presented an analytical methodology to model the kinetostatic behaviour of the mechanism that modelled the flexure hinges as having multiple degrees of freedom. The hinge stiffness in all degrees of freedom was obtained using either Paros-Weisbord equations or FEA. The 1-DOF micropositioning stage was used as a design example and the analytical model was compared to FEA, revealing 3.1% and 1.3% difference in the prediction of output displacement and stiffness, respectively. The models were experimentally verified, revealing that both models were within 10% of the experimental result.

Chang et al. (1999a) investigated a planar 3-DOF micropositioner for lithography, as shown in Figure 2-4. This consisted of a separate XY-stage, with low crosstalk interference, and a rotation stage, driven by 6 piezo-actuators in total. Each stage used a monolithic compliant mechanism with flexure beam elements. They derived

an analytical dynamic model based on a mass-spring-damper system with lumped parameters, as shown in Figure 2-14.

NOTE: This figure is included on page 50 of the print copy of the thesis held in the University of Adelaide Library.

Figure 2-14 - Schematic of dynamic model for $XY\theta_z$ micro-motion stage [Chang et al., 1999a].

The flexure beams were modelled as 1-DOF revolute joints with torsional springs and the links as rigid links. The piezo-actuator displacements were modelled as displacement elements and their dynamic behaviour as spring-dashpot elements. The Lagrangian method was used to derive the dynamic model. An ANSYS 3-D FEA model was also created. A direct comparison between the analytical model, FEA and experimental verification was also presented [Chang et al. 1999b]. This revealed that the analytical and FEA models were within 4.5% and 2.7%, respectively, for the translation displacement prediction and within 7.9% and 0.4%, respectively, for the rotation displacement prediction. The natural frequency prediction for the analytical and FEA models were within 3.3% and 7.1%, respectively, for the translational mode and within 8.2% and 7.4%, respectively, for the rotational mode.

Another model incorporating compliant mechanism and piezo-actuator was presented by Goldfarb and Celanovic (1999). They designed a gripper using a monolithic compliant mechanism with circular flexure hinges and driven by a stack piezo-actuator. They analysed the compliant mechanism using a PRBM type approach and also an FEA. The details and accuracy of this model were not discussed. However they also considered the modelling of the piezo-actuator and presented the quasi-static model of the actuator shown in Figure 2-13 (top). Figure 2-13 (bottom) depicts the operational area of the actuator.

This model does not present the non-linear hysteresis and dynamic behaviour of the piezo-actuator, but it does present the piezo-actuator characteristics that have a significant impact on the compliant mechanism design. The model was then incorporated with a compliant mechanism with compliant joints and rigid links as shown in Figure 2-15 (top). In this model the rotational joint stiffness k_j acts in parallel with the stiffness of the actuator. As seen in Figure 2-15 (bottom), the slope of the line defining the region of operation becomes k_p+k_j . It can be noted that the maximum no-load output displacement is limited, but the blocked output force is unchanged.

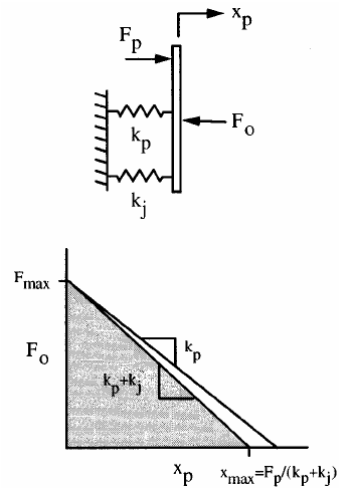


Figure 2-15 - (top) Quasi-static model of stack piezo-actuator with compliant mechanism joint stiffness and (bottom) region of operation.

Goldfarb and Celanovic also presented a model which included compliance in the structure due to link compliance and tensile, compressive and shear deformation of the flexure hinges. This was lumped into a single structural stiffness, k_s , which acts in series with the actuator as shown in Figure 2-16 (top). The slope of the line defining the operating area now becomes $(k_p + k_j) k_s / (k_p + k_j + k_s)$, which changes the blocked force but not the maximum no-load displacement, as shown in Figure 2-16 (bottom).

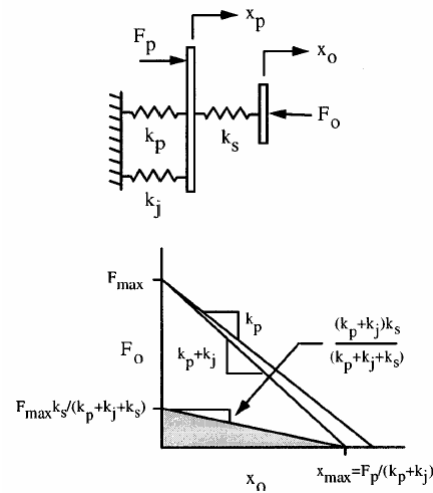


Figure 2-16 - (top) Quasi-static model of stack piezo-actuator with compliant mechanism joint stiffness structural compliance and (bottom) region of operation.

The effect on the compliant mechanism design when the piezo-actuator is included in the model has not been discussed in detail. But it is expected that the total micro-motion stage model will be significantly different to the compliant mechanism model in terms of the predicted output motion and natural frequency.

2.4 Optimal design of micro-motion stages

Numerous micro-motion stages have been designed using an optimal design approach. Commonly the optimisation has only considered the compliant mechanism and ignored the effect of the piezo-actuators on the design. Various compliant mechanism models have been used for optimal design. The validity of the optimal design will depend on the accuracy of the model and therefore the model used should have suitable accuracy. Models that have been used in optimisation are the PRBM, FEM and some other unique models.

2.4.1 Optimal design of a 1-DOF micro-motion stage

Chang and Du (1998) designed a 1-DOF flexure hinge compliant mechanism using a Scott-Russell amplification mechanism and used an ANSYS 2-D FEA to analysis the mechanism. They applied the Taguchi method to optimise the compliant mechanism parameters to achieve maximum displacement gain and minimum lateral displacement.

Elmustafa and Lagally (2001) developed 1-DOF nanopositioner for use with a CNC milling machine. The stage was a simple design with 4 flexural hinges (not notched) but no amplification of motion. This was to provide high stiffness and load capacity in both horizontal and vertical direction. FEA using ANSYS solid elements was applied leading to the redesign of the stage based on the specification of only two parameter variables. A static analysis was performed to produce graphs for the selection of design parameters to meet required performance characteristics.

As discussed earlier, Furukawa et al. (1995) developed a 1-DOF scanning stage and modelled both the compliant mechanism and the piezo-actuator. They also presented graphs of output displacement and natural frequency vs. the thickness of the flexure hinges, t . These graphs could be used to select the hinge thickness to give optimal desired performance. Two values of the flexure hinge radius, R , were also considered in this investigation.

Goldfarb and Celanovic [1999] discussed the implications of flexure hinge structure and piezo-actuator stiffness on the optimal design of their micro-gripper. However, they did not present any quantitative results.

Kang et al. (2004) considered the design, analysis and optimisation of planar compliant mechanisms using flexure hinges. They considered static performance measures such as task space stiffness and manipulability, subject to constraints such as joint stress, mechanism size, workspace volume and dynamic characteristics. They applied the multi-objective optimisation approach. The model they used for this analysis was a PRBM using a lumped approximation of flexure joints. They presented a 1-DOF stage model as an example of their approach.

Lobontiu and Garcia (2003) presented the optimisation of a 1-DOF notch flexure compliant amplification mechanism based on an analytical model using closed-loop equations. The procedure was based on Castigliano's displacement theorem and offered a simpler alternative to FEA. The output displacement, input stiffness and output stiffness of the amplification mechanism were calculated. An FEA model was used to confirm the new analytical model. A parametric study was performed for different linkage and hinge geometries. An optimisation procedure was proposed to provide an amplifier with optimal stiffness and displacement characteristics. The analytical optimised model was compared with the results of an FEA indicating less than 5% difference.

2.4.2 Optimal design of multiple degree of freedom micro-motion stages

Han et al. [1989, 1990] investigated the optimal design of their 6-DOF micromanipulator using a Stewart Platform. The analysis used a PRBM. They performed a kinematics and a force analysis to determine input torques, internal stresses and the deformation of critical members. A parameter sensitivity study was performed and graphs of parameter values vs. transmission ratio were presented. The synthesis of an optimum 4-bar linkage, considering minimum torque and stress and maximum motion range was performed. They also presented a design process flowchart to develop an optimal design. Castigliano's theorem was used to determine the stiffness of the flexure hinges and linear programming was used for the optimal design of the flexure hinges and legs, minimising the weight while constraining end-effector displacement, axial and buckling stress.

The modelling of a 3-DOF stage presented by Chang et al. (1999a) was discussed earlier. Using their analytical model they conducted a parametric analysis considering link lengths, hinge geometry and platform masses. The output performance characteristics measured were the output x- and y-axis displacements and rotation, and the natural frequency. An error budget analysis was used to determine the effect of manufacturing tolerances, material variation and hysteresis. The simulation results were effective to obtain a near-optimum design. Their model included the piezo-actuators.

Ohya et al. (1999) presented a brief parametric study of their spatial 3-DOF manipulator that considered just two linkage parameters. The output characteristic of

concern was the workspace area. Using the results of this study they selected parameters to maximise the workspace.

The 3-DOF spatial manipulator presented by Chung et al. (2001) was optimally designed to maximise isotropy. Using an analytical kinematic model based on a PRBM, they presented the global kinematic isotropic index. The greater this index the better the isotropy of the mechanism over the workspace. The linkage geometry was used in optimisation to maximise the global kinematic isotropic index. No mention was made of constraints or the optimisation method.

Culpepper et al. (2004) applied an optimal design approach to develop the 'HexFlex' 6-DOF nanomanipulator. The HexFlex was modeled using CoMeT™ (Compliant Mechanism Tool), a software written in Matlab. This models the kinematics and stiffness of the compliant mechanism. CoMeT uses the in-built Matlab sensitivity and optimisation routines to manipulate the matrix-based models and arrive at an optimal design.

Liu et al. (2001) used a PRBM based analysis of a compliant 6-DOF Stewart platform, shown in Figure 2-3, to define a physical model of the solution space. The parameters in this physical model are normalised hinge locations and link length. No details were given of the hinge modelling. They defined conditioning and stiffening indices to be used in optimal design. The conditioning indices are force, moment, linear velocity and angular velocity. The stiffness indices are position and orientation deformation. They then presented plots, or atlases, of these indices throughout the

solution space. Using these atlases the optimum geometry of the mechanism can be selected.

Tomita et al. (1992) presented a 6-DOF flexure hinge micromanipulator which was modelled using a PRBM approach. Kinematic and dynamic models were derived. A synthesis method was applied to decouple the degrees of freedom and increase the natural frequency to 170-180Hz. Experimental results were presented that were within 10% of theoretical prediction.

2.4.3 Optimal design of the 3RRR compliant mechanism

As yet there has been no reported study in which a 3RRR compliant mechanism has been optimally designed. The closest topology of mechanism to be optimally designed is the mechanism designed by Ryu et al. (1997), shown in Figure 2.8. In their work they optimally designed their compliant mechanism to maximise rotation. The modelling method was discussed earlier in this chapter. The optimisation parameters were individual hinge thickness and radius, link lengths and mechanism thickness. The constraints were maximum hinge stress, geometric size considerations, tilt stiffness and natural frequency. Sequential quadratic programming in Matlab was used to solve the optimisation problem. An experimental prototype was built using the optimised parameters, which revealed that theoretical and experimental results differ significantly. This was suggested to be due to decreased piezo-actuator displacement under load, machining error and modelling assumptions. The piezo-actuators were not considered in the optimisation.

2.5 Gaps in current knowledge

While the 3RRR compliant mechanism has received some attention it has still not been studied in great detail. Numerous gaps in the current knowledge have been identified.

2.5.1 Modelling of 3RRR compliant mechanism

It is not clear from the current literature, what modelling methods are most effective for the 3RRR compliant mechanism. No comparison has been made between a Pseudo-Rigid-Body-Model (PRBM) and any other, more accurate, methods to model the 3RRR compliant mechanism. It is not clear whether or not a PRBM may be useful in the optimal design of this mechanism, or what degree of error it would introduce. A PRBM has been used to accurately model a planar stage with different topology compliant mechanism [Chang, 1999], and if a PRBM can also provide sufficient accuracy to model the 3RRR compliant mechanism then this would be the simplest approach. This thesis will present a study comparing the PRBM to other modelling methods.

The analytical kinematic models based on the PRBM that have been previously derived [Zou, 2000], [Zhang et al., 2002] used a non-linear derivation and then linearised this using a Taylor series expansion. However, a linear approach could be applied from the beginning [Her and Chang, 1994], which would simplify the derivation. This thesis will present a linear analytical method to derive the kinematics and dynamics of the 3RRR compliant mechanism based upon a PRBM.

Previous research, of a compliant mechanism with topology similar to the 3RRR compliant mechanism, has applied a modelling method that uses analytical equations to model the multiple-degree-of-freedom compliance of the flexure hinges [Ryu, 1997]. However, no comparison has been made between such a modelling method and a Finite-Element-Model (FEM) or a PRBM. In this thesis, a model will be developed in ANSYS that uses analytical equations to model the multiple-degree-of-freedom compliance of the flexure hinges. Several different analytical equations available from the literature are considered for use in the model. The differences between them are highlighted, the equations which are the simplest to use are identified and the method to incorporate them into the model is discussed in detail. In the results a comparison is made between the predictions given by different analytical models and a FEM of the flexure hinge. This model also considers the compliance of the links, which has not been considered in previous models. The new model of the 3RRR compliant mechanism is compared to a FEM and the PRBM, and the models are then experimentally validated.

2.5.2 Modelling of $XY\theta_z$ micro-motion stage

From the current literature it has been found that only a few micro-motion stage designs have included the piezo-actuators into the stage model. As yet no stages using the 3RRR compliant mechanism have also considered the actuators in the design. It is well understood that the displacement of a piezo-actuator under load is less than the unloaded displacement. The stiffness of the compliant mechanism will affect the maximum displacement that can be achieved by the piezo-actuator, which in turn affects the maximum displacement of the stage. In addition, the stiffness of

the piezo-actuator will affect the micro-motion stage stiffness, which changes the natural frequency. These considerations will significantly affect the performance of the compliant mechanism. Therefore, to design a stage which can satisfy specific design requirements the piezo-actuator should be included into the model. This thesis presents a more complete $XY\theta_z$ micro-motion stage model, which includes both the 3RRR compliant mechanism and the piezo-actuators.

2.5.3 Workspace of the $XY\theta_z$ micro-motion stage

In the current literature there has only been presented one investigation into the workspace area of the 3RRR compliant mechanism [Handley, 2004b]. This investigation considered the 3RRR compliant mechanism only, rather than the complete $XY\theta_z$ stage. Furthermore, this investigation was based upon a PRBM, whose accuracy was not demonstrated, and considered only one configuration of compliant mechanism. This thesis will present a more thorough investigation of the workspace.

2.5.4 Optimal design of a $XY\theta_z$ micro-motion stage using the 3RRR compliant mechanism

As yet, a detailed parametric study of the 3RRR compliant mechanism, or $XY\theta_z$ stage using the 3RRR compliant mechanism, has not been performed and there is no clear understanding of how individual design parameters affect the behaviour of the stage. The results of a parametric study may provide design rules that would be useful to aid design and optimisation. Such a study is presented in this thesis. This

study uses both a PRBM and the model with multiple-degree-of-freedom compliance of the flexure hinges. It considers models of both the 3RRR compliant mechanism and the complete $XY\theta_Z$ stage.

As mentioned earlier, the 3RRR compliant mechanism offers unique advantages that can provide desirable control characteristics. Due to its symmetry it is relatively insensitive to thermal expansion errors; it can provide $XY\theta_Z$ motion with a very simple and light weight structure; and it can be designed to have decoupled stiffness. Decoupling design has not yet been applied in the design of a stage using the 3RRR compliant mechanism. Stiffness decoupling will be investigated in this thesis and considered as a constraint in the optimal design.

The optimal design of $XY\theta_Z$ stage using the 3RRR compliant mechanism has not yet been presented. A similar topology of compliant mechanism has only once been considered in optimal design [Ryu et al., 1997]. A different optimal design approach will be presented in this thesis. Furthermore, this optimal design will use a more complete $XY\theta_Z$ stage model, including the piezo-actuator model.

Chapter

3 Analytical modelling of the 3RRR compliant mechanism

In the literature review of chapter 2 several different micro-motion stages and modelling methods were presented. From this it can be observed that the easiest and most commonly applied method to model a flexure hinge based compliant mechanism is the pseudo-rigid-body model (PRBM). This method models notch flexure hinges, such as circular profile flexure hinges, as purely rotational joints with stiffness and the thick segments joining the hinges as rigid links. Well understood rigid-body analysis can then be applied to derive the kinematics and dynamics. In the literature review it was noted that the PRBM has limited accuracy as the flexure hinges do not deform to provide purely revolute motion, but also allow some translational motion. In cases where the compliant mechanism design is over-constrained, and hence a model describing a rigid-link mechanism with purely revolute joints could not move, axial deformation of the flexure hinges or links is required to enable the model of the mechanism to display translational motion. Modelling over constrained mechanisms using a PRBM has been shown to lead to errors of up to 30% compared to experimental results [Wu and Joungh 1998]. However, in other cases where the mechanism is not over constrained and the flexure

hinges are appropriately designed the error of the PRBM may be considerably less. In the literature it has not been demonstrated how accurately a PRBM can model the kinematics and dynamics of a 3RRR mechanism, or if a PRBM can be used in optimisation to give a useful design. Therefore the PRBM will be the first model type considered in this study. The PRBM can be derived using analytical modelling techniques that will be presented in this chapter.

3.1 PRBM analytical model

In the literature a number of approaches have been presented to derive a PRBM. In this chapter a new approach is presented that can be applied to any planar flexure hinge based compliant mechanism with small angle joint rotations. The rotation of a flexure hinge is limited by the elastic yield limit of the material and varies depending on the hinge profile. Circular profile flexure hinges give the least rotation [Lobontiu et al. 2002 (a)] compared to all other hinge profiles. Circular hinges made of metals allow rotations of less than 1 degree, and thus it will be assumed in this analysis that joint rotations are less than 1 degree. This method has been termed the ‘linear-Cartesian method’.

3.1.1 Linear-Cartesian method

The ‘linear-Cartesian method’ is a method of kinematic analysis that can be applied to mechanisms consisting of rigid links and revolute joints whose angular displacement is small. Micro-motion compliant mechanisms using notch flexure hinges typically have angular displacements of less than 1 degree and this method is

demonstrated to be appropriate for such cases. By applying a ‘lumped-mass approximation’ the linear-Cartesian can be extended to determine the dynamics of a mechanism. The method has been applied to planar mechanisms with single and multiple closed kinematic chains.

The linear-Cartesian method is similar to the linear scheme devised by Her and Chang (1994). However, the linear-Cartesian method uses Cartesian co-ordinates to locate joint positions rather than link lengths and angles. The length of the displaced linkage can then be determined by finding the difference in x and y position between points rather than taking a summation of x and y link components. This method is computationally simpler than the Her and Chang method, particularly for multiple loop mechanisms with many joints. It is also easier to apply, as the geometric constraint equations are simpler to derive. In their paper the Her and Chang method was applied for kinematic analysis only, but not extended to dynamics.

The linear-Cartesian method will be applied to derive both the kinematic and dynamic models for a compliant four-bar linkage and a 3RRR compliant mechanism.

3.1.2 Flexure hinge model

For this PRBM analysis the flexure hinge, as shown in Figure 3-1(a), will be modelled as a revolute joint with torsional spring, as shown in Figure 3-1(b).

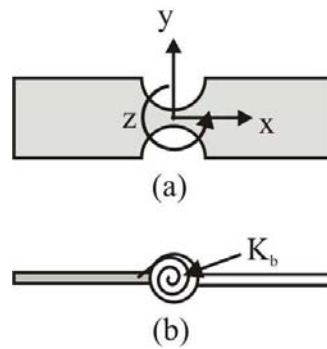


Figure 3-1 - (a) Flexure hinge and (b) a PRBM representation of the flexure hinge.

The hinge will be defined to have rotation about the z -axis. The parameters defining the hinge geometry are shown in Figure 3-2.

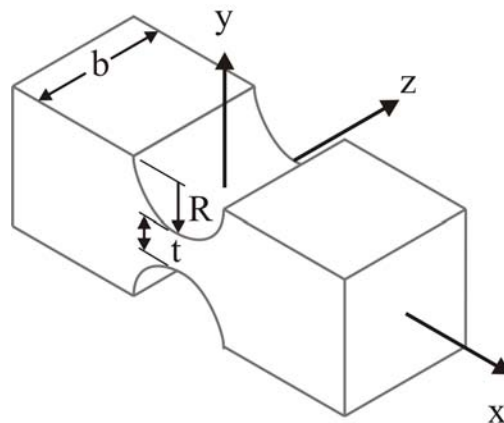


Figure 3-2 - Parameters defining flexure hinge geometry.

The stiffness in bending of the hinge is given by K_b , which will be calculated using the analytical equation given in equation (3.1) [Wu, 2002]. This gives the same stiffness as the commonly used equation of Paros and Weisbord (1965).

$$K_b = 1 / \left[\frac{12}{EbR^2} \left[\frac{2s^3(6s^2 + 4s + 1)}{(2s + 1)(4s + 1)^2} + \frac{12s^4(2s + 1)}{(4s + 1)^{5/2}} \arctan \sqrt{4s + 1} \right] \right] \quad (3.1)$$

where E is the Young's modulus of the material and

$$s = R/t \quad (3.2)$$

3.2 Four-bar linkage model

The proposed method is first demonstrated by the example of a compliant four-bar linkage. The linkage shown in Figure 3-3 is a general four-bar linkage with an arbitrarily chosen geometry. It is used for illustrative purposes only and has no specific practical use. The flexure hinges are assumed to provide revolute motion only and therefore the movement of the mechanism is kinematically constrained. It is assumed that the angular displacement of any joint in this mechanism will be less than 1 degree.

3.2.1 Kinematic model

This compliant mechanism can be modelled using a PRBM as shown in Figure 3-3. The flexure hinges are modelled as revolute joints with torsional stiffness. At this point only the kinematic model will be discussed and the dynamic effect of the joint stiffness will be ignored. The dynamic model will be discussed in the following section.

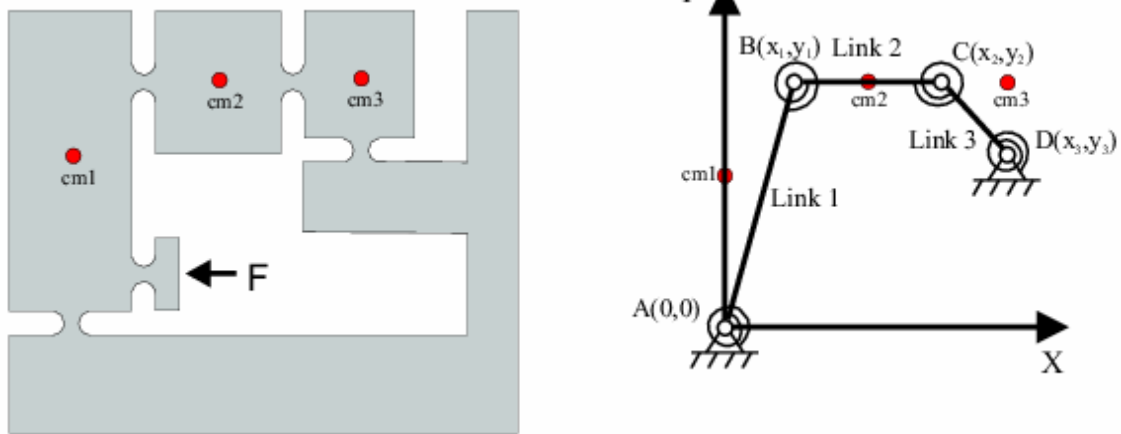


Figure 3-3- A compliant four-bar linkage and its pseudo-rigid-body-model. The dots indicate the centre of mass of the links.

To begin, consider a single link rotating through a small angle, as shown in Figure 3-4. Point B is the free end of the link and is defined by its x and y coordinate as given in equations (3.3) and (3.4).

$$x_1 = R_1 \cos \theta_1 \tag{3.3}$$

$$y_1 = R_1 \sin \theta_1 \tag{3.4}$$

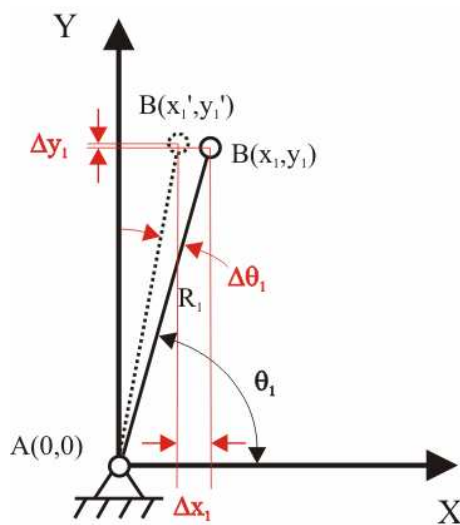


Figure 3-4 - A single link rotating through a small angle.

If link 1 is displaced by a small change in joint angle $\Delta\theta_1$ then the new coordinates are given by equations (3.5) and (3.6).

$$x_1' = R_1 \cos(\theta + \Delta\theta_1) = R_1 (\cos\theta_1 \cos\Delta\theta_1 - \sin\theta_1 \sin\Delta\theta_1) \quad (3.5)$$

$$y_1' = R_1 \sin(\theta + \Delta\theta_1) = R_1 (\sin\theta_1 \cos\Delta\theta_1 + \cos\theta_1 \sin\Delta\theta_1) \quad (3.6)$$

Using the small angle assumptions $\cos(\Delta\theta) \approx 1$, $\sin(\Delta\theta) \approx \Delta\theta$ and subtracting the original coordinate gives the change in coordinate to be equations (3.7) and (3.8).

$$\Delta x_1 = x_1' - x_1 \approx R_1 [\cos\theta_1 - \sin\theta_1 (\Delta\theta_1)] - R_1 \cos\theta_1 = -(\Delta\theta_1) R_1 \sin\theta_1 = -\Delta\theta_1 y_1 \quad (3.7)$$

$$\Delta y_1 = y_1' - y_1 \approx R_1 [\sin\theta_1 + \cos\theta_1 (\Delta\theta_1)] - R_1 \sin\theta_1 = (\Delta\theta_1) R_1 \cos\theta_1 = \Delta\theta_1 x_1 \quad (3.8)$$

It can be seen from equations (3.7) and (3.8) that the displacement of point B in the x-direction is given by the product of the change in angle and the initial distance in the y-direction between B and the centre of rotation of the link. Likewise the y displacement is the product of the change in angle and the initial x-distance between point B and centre of rotation. This basic approach can be further extended to analyse the case of multiple links.

Consider the four-bar linkage in Figure 3-5. It is momentarily assumed that point D, is detached from the ground. The total displacement of point D due to a change in angle of all joints is given by a sum of displacements, as given in equations (3.9) and (3.10), where the values of x_i and y_i ($i=1,2,3$) are the Cartesian co-ordinates of the joints. Point D is of course actually constrained and thus has zero displacement. Therefore equations (3.9) and (3.10) equate to zero. These are the geometric constraint equations.

$$\Delta x_3 = -[(\Delta\theta_1)(y_3 - 0) + (\Delta\theta_2)(y_3 - y_1) + (\Delta\theta_3)(y_3 - y_2)] = 0 \quad (3.9)$$

$$\Delta y_3 = (\Delta\theta_1)(x_3 - 0) + (\Delta\theta_2)(x_3 - x_1) + (\Delta\theta_3)(x_3 - x_2) = 0 \quad (3.10)$$

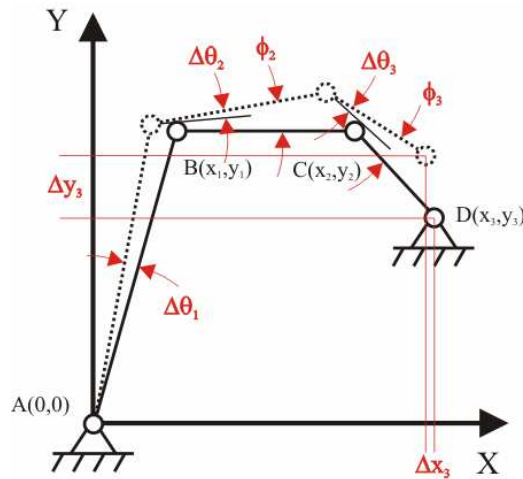


Figure 3-5 - A four-bar linkage with each joint rotating through a small angle.

We now have two linear kinematic constraint equations. The input to the four-bar linkage is a displacement of one link, say $\Delta\theta_1$, and we have two unknown

displacements, $\Delta\theta_2$ and $\Delta\theta_3$. These two equations can be solved easily to provide both $\Delta\theta_2$ and $\Delta\theta_3$ as a product of $\Delta\theta_1$ and a constant.

The total change in angle of link 2 is given by adding the rotation of links 1 and 2, and the total change in angle of link 3 is given by adding the rotation links 1, 2 and 3, as given by equations (3.11) and (3.12), respectively.

$$\phi_2 = \Delta\theta_1 + \Delta\theta_2 = c_2\Delta\theta_1 \quad (3.11)$$

$$\phi_3 = \Delta\theta_1 + \Delta\theta_2 + \Delta\theta_3 = c_3\Delta\theta_1 \quad (3.12)$$

where c_2 and c_3 are constants. Equations (3.11) and (3.12) are the kinematic equations describing the four-bar linkage. As the kinematic equations are linear, the Jacobian, which is the time derivative of the kinematic equations, is described by the similar linear equations, as given by equations (3.13) and (3.14).

$$\dot{\phi}_2 = c_2 \dot{\theta}_1 \quad (3.13)$$

$$\dot{\phi}_3 = c_3 \dot{\theta}_1 \quad (3.14)$$

3.2.2 Dynamic model

The general form of the dynamic model is given by equation (3.15).

$$M(\theta_1)\ddot{\theta}_1 + C(\theta_1, \dot{\theta}_1)\dot{\theta}_1 + K(\theta_1) = \tau \quad (3.15)$$

Where $M(\theta_l)$ is the inertia term, $C(\theta_l, \dot{\theta}_l)$ is the centripetal term, $K(\theta_l)$ is the stiffness term and τ is the forcing term.

To derive the dynamic model the Lagrangian method can be applied. The Lagrangian equation is given in equation (3.16) below.

$$\frac{d}{dt} \frac{\partial K}{\partial \dot{\theta}_1} - \frac{\partial K}{\partial \theta_1} + \frac{\partial P}{\partial \theta_1} = \tau \quad (3.16)$$

Where K is the kinetic energy term and P is the potential energy term.

3.2.2.1 Potential energy

The potential energy of the mechanism is stored in the stiffness of the flexure hinges. Gravity is ignored in this analysis as it is generally far less significant than the stiffness of the structure, as link and load masses are generally relatively small. The bending stiffness of the flexure hinges, K_b , can be calculated using equation (3.1).

The potential energy of the four-bar linkage is given by equation (3.17).

$$P = \frac{1}{2} \sum_{i=1}^4 k_i \Delta \theta_i^2 = \frac{1}{2} [k_1 \Delta \theta_1^2 + k_2 \Delta \theta_2^2 + k_3 \Delta \theta_3^2 + k_4 \Delta \theta_4^2] \quad (3.17)$$

where k_1 , k_2 , k_3 and k_4 , are the stiffnesses of flexure hinges A, B, C and D, respectively, and the flexure hinge rotations are given by equations (3.18) to (3.20).

$$\Delta\theta_2 = \phi_2 - \Delta\theta_1 = c_2\Delta\theta_1 - \Delta\theta_1 = (c_2 - 1)\Delta\theta_1 \quad (3.18)$$

$$\Delta\theta_3 = \phi_3 - \phi_2 = c_3\Delta\theta_1 - c_2\Delta\theta_1 = (c_3 - c_2)\Delta\theta_1 \quad (3.19)$$

$$\Delta\theta_4 = \phi_3 = c_3\Delta\theta_1 \quad (3.20)$$

Substituting equations (3.18) to (3.20) into equation (3.17) gives the potential energy as a function of $\Delta\theta_1$, equation (3.21). All other values are constants and, therefore, the equation can be represented as in equation (3.22) where Ψ is a constant.

$$P = \frac{1}{2} [k_1 + k_2(c_2 - 1)^2 + k_3(c_3 - c_2)^2 + k_4c_3^2] \Delta\theta_1^2 \quad (3.21)$$

$$P = \frac{1}{2} \Psi \Delta\theta_1^2 \quad (3.22)$$

To calculate the stiffness term of the Lagrangian we take the partial derivative of P, as given in equation (3.23).

$$\frac{\partial P}{\partial \theta_1} = \frac{\partial \left(\frac{1}{2} \Psi \Delta\theta_1^2 \right)}{\partial \theta_1} = \frac{\partial \left(\frac{1}{2} \Psi (\theta_1 - \theta_{1o})^2 \right)}{\partial \theta_1} = \Psi (\theta_1 - \theta_{1o}) = \Psi \Delta\theta_1 \quad (3.23)$$

3.2.2.2 Kinetic energy

A lumped-mass approximation is used in this model, i.e. the mass of the links is assumed to be a point mass located at the centre of mass as shown in Figure 3-3. The kinetic energy of the mechanism is given by equation (3.24).

$$K = \sum_{i=1}^3 \left[\frac{1}{2} m_i (V_{ix}^2 + V_{iy}^2) + \frac{1}{2} J_i \dot{\theta}_i^2 \right] \quad (3.24)$$

where V is the velocity of the centre of mass of the links, m is the mass of the links and J is the moment of inertia of the links.

V_x and V_y for each link can be determined using the Jacobian constants, equations (3.13) and (3.14), and by applying the same approach as was used to generate the constraint equations, equations (3.9) and (3.10). As all the terms other than link displacements are constants $\Delta\theta_1$, $\Delta\theta_2$ and $\Delta\theta_3$ can be replaced with $\dot{\theta}_1$, $\dot{\theta}_2$ and $\dot{\theta}_3$, respectively.

$$V_{1x} = \dot{\theta}_1 (cm1_y - 0) = V_{c1x} \dot{\theta}_1 \quad (3.25)$$

$$V_{1y} = -\dot{\theta}_1 (cm1_x - 0) = V_{c1y} \dot{\theta}_1 \quad (3.26)$$

$$V_{2x} = \dot{\theta}_1 (cm2_y - A_y) + c_2 \dot{\theta}_1 (cm2_y - B_y) = V_{c2x} \dot{\theta}_1 \quad (3.27)$$

$$V_{2y} = -\dot{\theta}_1(cm_{2x} - A_x) + c_2 \dot{\theta}_1(cm_{2x} - B_x) = Vc_{2y} \dot{\theta}_1 \quad (3.28)$$

$$V_{3x} = c_3 \dot{\theta}_1(cm_{3y} - D_y) \quad (3.29)$$

$$V_{3y} = -c_3 \dot{\theta}_1(cm_{3x} - D_x) \quad (3.30)$$

These velocity terms, equations (3.25) to (3.30) can be substituted into the kinetic energy equation, equation (3.24). The mass moment of inertia of each link, J , which is dependent on the shape of the link, can also be substituted into the kinetic energy equation.

If the link is rectangular, with height, h , and width, b , then J is given by equation (3.31) below.

$$J_i = \frac{1}{12} m_i (b_i^2 + h_i^2) \quad , \quad i=1,2,3 \quad (3.31)$$

The resulting equation can be written as a function of $\dot{\theta}_1$ where all other values are constants, equation (3.32). The kinetic energy equation can thus be represented in the form of equation (3.33) where Ω is a constant.

$$K = \frac{1}{2} [m_1 (Vc_{1x}^2 + Vc_{1y}^2) + J_1 + m_2 (Vc_{2x}^2 + Vc_{2y}^2) + J_2 + m_3 (Vc_{3x}^2 + Vc_{3y}^2) + J_3] \dot{\theta}_1^2 \quad (3.32)$$

$$K = \frac{1}{2} \Omega \dot{\theta}_1^2 \quad (3.33)$$

To obtain the Lagrangian terms we take two derivatives. The first is equation (3.34).

$$\frac{d}{dt} \frac{\partial K}{\partial \dot{\theta}_1} = \frac{d}{dt} \frac{\partial \left(\frac{1}{2} \Omega \dot{\theta}_1^2 \right)}{\partial \dot{\theta}_1} = \frac{d}{dt} \Omega \dot{\theta}_1 = \Omega \ddot{\theta}_1 \quad (3.34)$$

The second is equation (3.35).

$$\frac{\partial K}{\partial \theta_1} = \frac{\partial \left(\frac{1}{2} \Omega \dot{\theta}_1^2 \right)}{\partial \theta_1} = 0 \quad (3.35)$$

Looking at the kinetic energy term it can be seen that this is a function of velocity only. Therefore the derivative with respect to displacement is zero and there is no centripetal term. If one considers the nature of this linear model it can be reasoned why this is the case. The angular motion of each joint is neglected when the small angle assumption is made. As the motion of each joint is linear no angular centripetal forces are generated.

Substituting equations (3.23), (3.34) and (3.35) into equation (3.16) gives the total dynamic model for the four-bar linkage as given in equation (3.36).

$$\Omega \ddot{\theta}_1 + \Psi \theta_1 = \tau \quad (3.36)$$

Thus the dynamic model is given by a linear ordinary differential equation with constant coefficients.

3.2.3 Comparison of linear model and complete non-linear model

To demonstrate the accuracy of a model derived using the linear-Cartesian method it was compared to a general non-linear PRBM. The non-linear model was derived for the four-bar linkage using the Lagrangian method. The details of this model are given in [Zhang, 1999]. This model has the form given in equation (3.37).

$$M(\theta_1)\ddot{\theta}_1 + C(\theta_1, \dot{\theta}_1)\dot{\theta}_1 + K(\theta_1) = \tau \quad (3.37)$$

The linear model is far simpler than the general non-linear model, and has the form given in equation (3.38).

$$M_{lin}\Delta\ddot{\theta}_1 + K_{lin}\Delta\theta_1 = \tau \quad (3.38)$$

To compare both models, the four-bar linkage shown in Figure 3-6 is considered next. The parameters defining this linkage are given in Table 3-1.

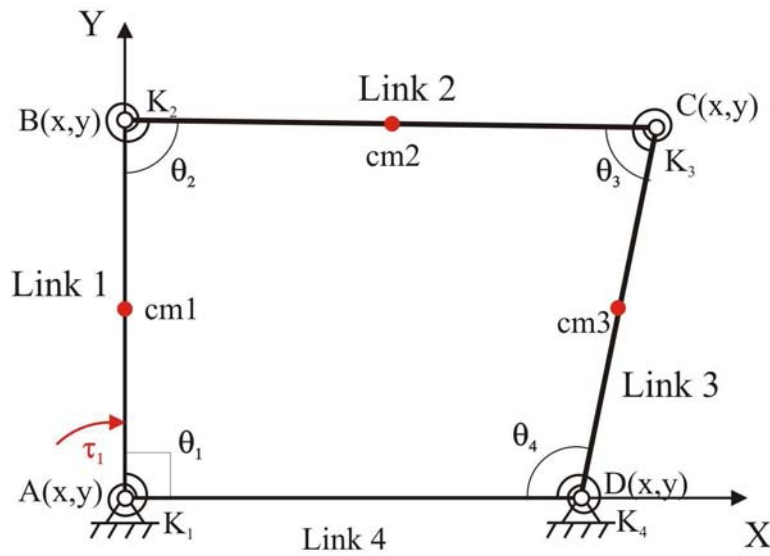


Figure 3-6 – A schematic of the example compliant four-bar linkage.

Four-Bar Linkage Parameter	Value
Length - Link 1, Link 2, Link 3, Link 4 (mm)	50, 70, 50, 60
$\theta_1, \theta_2, \theta_3, \theta_4$ (°)	90, 89.17, 78.47, 102.35
$A(x,y), B(x,y), C(x,y), D(x,y)$ (mm)	(0,0), (0,50), (69.99,48.99), (60, 0)
Mass - Link 1, Link 2, Link 3 (g)	10, 500, 10
K_1, K_2, K_3, K_4 (Nm/rad)	40
τ_1 (Nm)	1.2

Table 3-1 - Example four-bar Linkage Parameters.

3.2.3.1 Kinematics

To compare the kinematics of both models an input angular displacement, $\Delta\theta_1$ of 1° was applied to link 1 of both models. The rotational displacements of the other joints, $\Delta\theta_2$, $\Delta\theta_3$, and $\Delta\theta_4$ generated by this input were then calculated.

The linear-Cartesian method was used to calculate the linear kinematic constants, c_2 and c_3 , as defined in equations (3.13) and (3.14). These constants are given below.

$$c_2 = 0.1453 \quad (3.39)$$

$$c_3 = 1.0176 \quad (3.40)$$

The values of constants c_2 and c_3 are substituted into equations (3.18) to (3.20) to calculate the rotational displacements of the joints. The non-linear model was used to calculate the same rotational displacements. The results from both models are given in Table 3-2.

Joint Angle	Linear-Cartesian Model $\Delta\theta$ (°)	Non-linear Model $\Delta\theta$ (°)	Difference (%)
θ_1	1	1	0
θ_2	-0.8547	-0.8550	0.04
θ_3	0.8723	0.8711	0.14
θ_4	-1.0176	-1.0160	0.16

Table 3-2 - Angular displacement of joints predicted by linear and non-linear kinematic models.

It can be seen that the linear and non-linear models give very similar results.

3.2.3.2 Dynamics

Using the linear-Cartesian method the dynamic model was derived for the example four-bar linkage. This is given in equation (3.41) below.

$$0.0014\ddot{\theta}_1 + 141.1\theta_1 = \tau \quad (3.41)$$

To compare this linear dynamic model with the non-linear model, a step input torque, $\tau_1=1.2$ Nm, was applied to link 1 of both models. This caused oscillation of the four-bar linkage with an amplitude of $\Delta\theta_1 = 0.97^\circ$. The non-linear model inertia term,

$M(\theta_l)$, centripetal term, $C(\theta_l, \dot{\theta}_l)$, and stiffness term, $K(\theta_l)$, were compared to their respective counterparts, M_{lin} , and $K_{lin}\Delta\theta_l$. This comparison was made at the two extreme positions of the four-bar linkage, i.e. at $\Delta\theta_l = 0^\circ$ and 0.97° . The parameters of the dynamic model are shown in Table 3-3.

$\Delta\theta_l$	0°	0.97°
M	0.0014	0.0014
M_{lin}	0.0014	0.0014
C	1.22E-04	1.23E-04
K($\Delta\theta$)	0	2.396
K_{lin}$\Delta\theta$	0	2.398

Table 3-3 - Comparison of dynamic model terms for $\Delta\theta_l = 0^\circ$ and 0.97° .

From these results it is apparent that the non-linear terms do not vary significantly for this small-scale motion. The inertia terms are identical, the C term is negligible, and the stiffness terms are nearly identical. This result demonstrates that the ‘linear-Cartesian’ method is a valid approximation for the PRBM of the four-bar linkage, with accuracy close to a non-linear PRBM.

3.3 3RRR compliant mechanism

In the previous section the ‘linear-Cartesian’ method was applied to a single loop micro-motion compliant mechanism. It was demonstrated that the performance of both the kinematic and the dynamic model are very close to the original non-linear model. The method is now applied to the multiple loop case of the 3RRR compliant mechanism, as shown in Figure 3-7 with its PRBM.

Considering the 3RRR mechanism it can be seen that there are three closed loops. However, as will be demonstrated, only two of these need be considered in order to determine the kinematics of the mechanism. Three inputs must be defined to determine the position of the end-effector of the mechanism. The inputs to the mechanism are the rotations of joints A_1 , A_2 and A_3 given by $\Delta\theta_{A_1}$, $\Delta\theta_{A_2}$ and $\Delta\theta_{A_3}$.

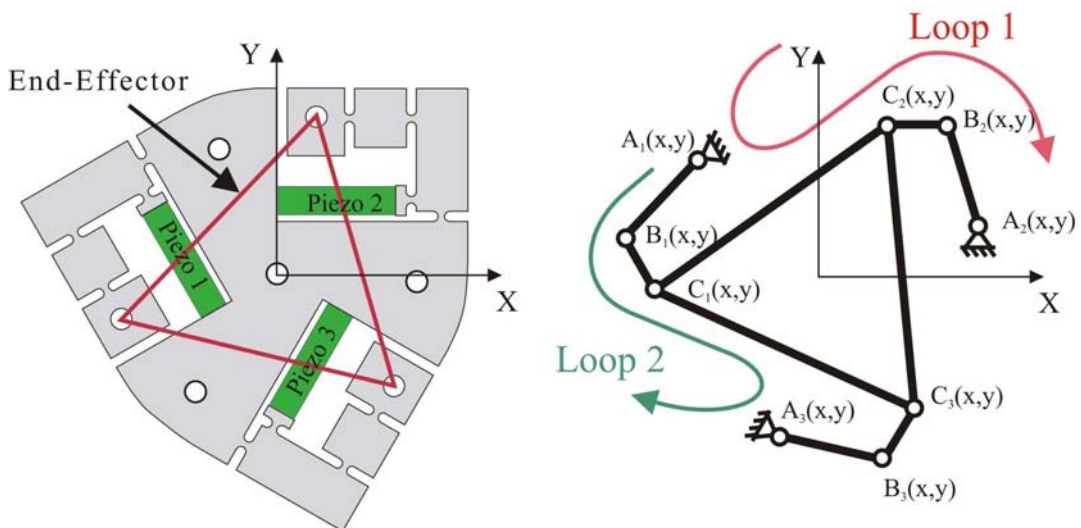


Figure 3-7 -Schematic of the 3RRR compliant mechanism and its PRBM.

The geometry of the mechanism is described using the Cartesian coordinates of the joints. These coordinate values are then used directly in the constraint equations to give the distance between the end-points of each link and the centres of rotation. The points describing the joint locations can be defined using a global Cartesian reference frame of any orientation. The solution for the unknown angular joint displacements will be the same regardless of the orientation of the reference frame. However, it is most convenient to describe the joint locations of one linkage, say linkage 2, using the global reference frame shown in Figures 3-7 and 3-10. The joint locations of linkage 1 and 3 can then be found by rotating linkage 2 through 120° and 240° , respectively. The origin of the reference frame describing the joint locations coincides with the centre of the end-effector.

The geometric parameters used to define the 3RRR linkages are shown in Figure 3-8.

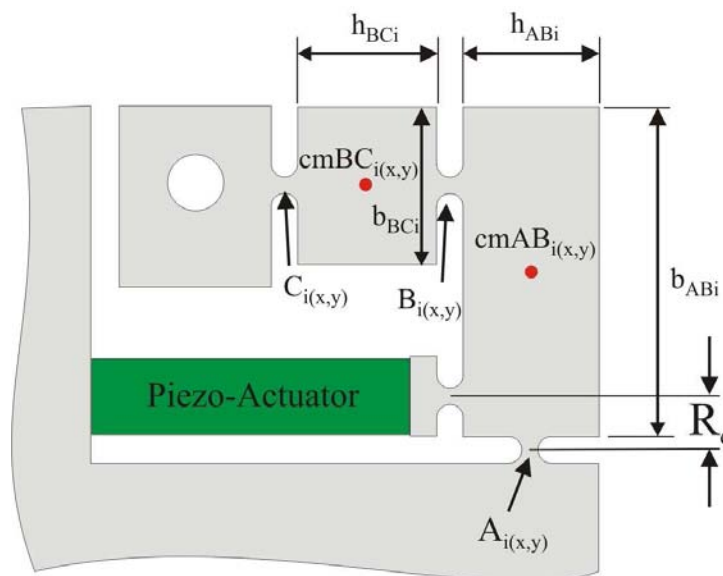


Figure 3-8 - Diagram showing the geometric parameters defining the 3RRR linkages ($i=1,2,3$).

3.3.1 Kinematic model

The kinematic constraint equations for loop 1 are:

$$\begin{aligned} \Delta x(loop1) = & \Delta\theta_{A1}(A_{2y} - A_{1y}) + \Delta\theta_{B1}(A_{2y} - B_{1y}) + \Delta\theta_{c1}(A_{2y} - C_{1y}) + \Delta\theta_{C2}(A_{2y} - C_{2y}) \\ & + \Delta\theta_{B2}(A_{2y} - B_{2y}) = 0 \end{aligned} \quad (3.42)$$

$$\begin{aligned} \Delta y(loop1) = & -(\Delta\theta_{A1}(A_{2x} - A_{1x}) + \Delta\theta_{B1}(A_{2x} - B_{1x}) + \Delta\theta_{c1}(A_{2x} - C_{1x}) + \\ & \Delta\theta_{C2}(A_{2x} - C_{2x}) + \Delta\theta_{B2}(A_{2x} - B_{2x})) = 0 \end{aligned} \quad (3.43)$$

The kinematic constraint equations for loop 2 are:

$$\begin{aligned} \Delta x(loop2) = & \Delta\theta_{A1}(A_{3y} - A_{1y}) + \Delta\theta_{B1}(A_{3y} - B_{1y}) + \Delta\theta_{c1}(A_{3y} - C_{1y}) + \Delta\theta_{C3}(A_{3y} - C_{3y}) \\ & + \Delta\theta_{B3}(A_{3y} - B_{3y}) = 0 \end{aligned} \quad (3.44)$$

$$\begin{aligned} \Delta y(loop2) = & -(\Delta\theta_{A1}(A_{3x} - A_{1x}) + \Delta\theta_{B1}(A_{3x} - B_{1x}) + \Delta\theta_{c1}(A_{3x} - C_{1x}) + \Delta\theta_{C3}(A_{3x} - C_{3x}) \\ & + \Delta\theta_{B3}(A_{3x} - B_{3x})) = 0 \end{aligned} \quad (3.45)$$

Inputs to the mechanism are $\Delta\theta_{A1}$, $\Delta\theta_{A2}$ and $\Delta\theta_{A3}$, while $\Delta\theta_{B2}$ and $\Delta\theta_{B3}$ are given by equations (3.46) and (3.47) respectively.

$$\Delta\theta_{B2} = \Delta\theta_{A2} - (\Delta\theta_{A1} + \Delta\theta_{B1} + \Delta\theta_{C1} + \Delta\theta_{C2}) \quad (3.46)$$

$$\Delta\theta_{B3} = \Delta\theta_{A3} - (\Delta\theta_{A1} + \Delta\theta_{B1} + \Delta\theta_{C1} + \Delta\theta_{C3}) \quad (3.47)$$

Equations (3.46) and (3.47) can be substituted into the four loop equations, equations (3.42) to (3.45). There are now four unknowns, $\Delta\theta_{B1}$, $\Delta\theta_{C1}$, $\Delta\theta_{C2}$ and $\Delta\theta_{C3}$. Therefore, the four linear equations can be solved simultaneously to find the four

unknowns. Each displacement is given as a function of the 3 input rotations $\Delta\theta_{A1}$, $\Delta\theta_{A2}$ and $\Delta\theta_{A3}$.

Furthermore the input rotations $\Delta\theta_{A1}$, $\Delta\theta_{A2}$ and $\Delta\theta_{A3}$ are given by equation (3.48).

$$\Delta\theta_{Ai} = -\frac{\Delta L_i}{R_o}, \quad i = 1,2,3 \quad (3.48)$$

where ΔL_i is the displacement of the i^{th} piezo-actuator and R_o is described in Figure 3-8. In this model it is assumed that all of the elongation of the piezo-actuators is transferred to the compliant mechanism. However, in later Chapters it will be established that in the real system this may not be the case.

The kinematics of the end-effector motion can be calculated using equations (3.49) to (3.51). The subscript ‘Z’ in equation 3.51 refers to the Z-axis, which is perpendicular to the X-Y plane.

$$X = \Delta\theta_{A1}(0 - A_{1y}) + \Delta\theta_{B1}(0 - B_{1y}) + \Delta\theta_{c1}(0 - C_{1y}) \quad (3.49)$$

$$Y = -(\Delta\theta_{A1}(0 - A_{1x}) + \Delta\theta_{B1}(0 - B_{1x}) + \Delta\theta_{c1}(0 - C_{1x})) \quad (3.50)$$

$$\theta_Z = \phi_{C1} = \Delta\theta_{A1} + \Delta\theta_{B1} + \Delta\theta_{C1} \quad (3.51)$$

The resulting kinematics is described by a 3x3 matrix of constants, which is multiplied by the input piezo-actuator displacement to give the end-effector motion, as given in equation (3.52).

$$\begin{bmatrix} \Delta X \\ \Delta Y \\ \Delta \theta_z \end{bmatrix} = \begin{bmatrix} J_{11} & J_{12} & J_{13} \\ J_{21} & J_{22} & J_{23} \\ J_{31} & J_{32} & J_{33} \end{bmatrix} \begin{bmatrix} \Delta L_1 \\ \Delta L_2 \\ \Delta L_3 \end{bmatrix} \quad (3.52)$$

The parametric values of these nine constants are given in Appendix A.1. The Jacobian is given by the same constant matrix.

3.3.2 Dynamic model

The dynamic model is derived using the same approach, using the Lagrangian method, as described in the four-bar case. However, in this case partial derivatives are taken of kinetic and potential energy with respect to three piezo-actuator displacements and velocities, L_1 , L_2 and L_3 , and \dot{L}_1 , \dot{L}_2 , and \dot{L}_3 . There are also three input forces F_1 , F_2 and F_3 , giving the Lagrangian in equation (3.53).

$$\frac{d}{dt} \frac{\partial K}{\partial \dot{L}_i} - \frac{\partial K}{\partial L_i} + \frac{\partial P}{\partial L_i} = \begin{bmatrix} F_1 \\ F_2 \\ F_3 \end{bmatrix}, \quad i=1,2,3 \quad (3.53)$$

The potential energy term is given by equation (3.54).

$$P = \frac{1}{2} \left[\sum_{i=1}^3 k_i \Delta \theta_{Ai}^2 + \sum_{j=1}^3 k_j \Delta \theta_{Bj}^2 + \sum_{n=1}^3 k_n \Delta \theta_{Cn}^2 \right] \quad (3.54)$$

where the k terms are the flexure hinge bending stiffnesses as given by equation (3.1) and the $\Delta\theta$ terms are the flexure hinge rotations found using equations (3.42) to (3.48).

Calculating the total potential energy results in an equation of the form given in equation (3.55)

$$P = \alpha L_1^2 + \alpha L_2^2 + \alpha L_3^2 + \beta L_1 L_2 + \beta L_1 L_3 + \beta L_2 L_3 \quad (3.55)$$

where α and β are constants. They are discussed further in Appendix A.2. Taking the partial derivatives of the potential energy with respect to the piezo-actuator input displacement leads to equation (3.56).

$$\frac{\partial P}{\partial L_i} = \begin{bmatrix} 2\alpha & \beta & \beta \\ \beta & 2\alpha & \beta \\ \beta & \beta & 2\alpha \end{bmatrix} \begin{bmatrix} L_1 \\ L_2 \\ L_3 \end{bmatrix} \quad (3.56)$$

The kinetic energy is given by equation (3.57).

$$K = \frac{1}{2} \left[\begin{array}{l} m_{ee} (V_{eex}^2 + V_{eey}^2) + J_{ee} \dot{\theta}_{ee}^2 + \\ \sum_{i=1}^3 [m_{ABi} (V_{ABix}^2 + V_{ABiy}^2) + J_{ABi} \dot{\theta}_{ABi}^2 + m_{BCi} (V_{BCix}^2 + V_{BCiy}^2) + J_{BCi} \dot{\theta}_{BCi}^2] \end{array} \right] \quad (3.57)$$

Where the subscript ‘ee’ refers to the end-effector, ‘AB’ refers to link AB and ‘BC’ refers to link BC.

The end-effector velocities, V_{eex} and V_{eey} , are given directly by the Jacobian, while the moment of inertia for a thin triangle is given by equation (3.58).

$$J_{ee} = \frac{1}{9} m_{ee} h_{ee}^2 \quad (3.58)$$

In this equation m_{ee} is the end-effector mass and h_{ee} is the height of the triangle.

The velocity and moment of inertia of link AB_i ($i=1,2,3$) is given by equations (3.59)- (3.61).

$$V_{ABix} = \dot{\theta}_{Ai} (cmAB_{iy} - A_{iy}) \quad (3.59)$$

$$V_{ABiy} = -\dot{\theta}_{Ai} (cmAB_{ix} - A_{ix}) \quad (3.60)$$

$$J_{ABi} = \frac{1}{12} m_{ABi} (b_{ABi}^2 + h_{ABi}^2) \quad (3.61)$$

The velocity and moment of inertia of link BC_i , $i=1,2,3$ is given by equations (3.62)-(3.64).

$$V_{BC_{ix}} = \dot{\theta}_{A_i}(cmBC_{iy} - A_{iy}) + \dot{\theta}_{B_i}(cmBC_{iy} - B_{iy}) \quad (3.62)$$

$$V_{BC_{iy}} = -\dot{\theta}_{A_i}(cmBC_{ix} - A_{ix}) + \dot{\theta}_{B_i}(cmBC_{ix} - B_{ix}) \quad (3.63)$$

$$J_{BC_i} = \frac{1}{12} m_{BC_i} (b_{BC_i}^2 + h_{BC_i}^2) \quad (3.64)$$

All angular velocities, $\dot{\theta}$, are functions of \dot{L}_1 , \dot{L}_2 , and \dot{L}_3 . Calculating the total kinetic energy results in an equation of the form given in equation (3.65).

$$K = \psi \dot{L}_1^2 + \psi \dot{L}_2^2 + \psi \dot{L}_3^2 + \sigma \dot{L}_1 \dot{L}_2 + \sigma \dot{L}_1 \dot{L}_3 + \sigma \dot{L}_2 \dot{L}_3 \quad (3.65)$$

where ψ and σ are constants. They are discussed further in Appendix A.2.

To obtain the Lagrangian terms two derivatives are taken. The first is equation (3.66) below.

$$\frac{d}{dt} \frac{\partial K}{\partial \dot{\theta}_1} = \begin{bmatrix} 2\psi & \sigma & \sigma \\ \sigma & 2\psi & \sigma \\ \sigma & \sigma & 2\psi \end{bmatrix} \begin{bmatrix} \ddot{L}_1 \\ \ddot{L}_2 \\ \ddot{L}_3 \end{bmatrix} \quad (3.66)$$

The second is equation (3.67) below.

$$\frac{\partial K}{\partial L_i} = 0 \quad (3.67)$$

Substituting equations (3.56), (3.66) and (3.67) into equation (3.53) gives the total dynamic model for the 3RRR mechanism as equation (3.68).

$$\begin{bmatrix} 2\psi & \sigma & \sigma \\ \sigma & 2\psi & \sigma \\ \sigma & \sigma & 2\psi \end{bmatrix} \begin{bmatrix} \ddot{L}_1 \\ \ddot{L}_2 \\ \ddot{L}_3 \end{bmatrix} + \begin{bmatrix} 2\alpha & \beta & \beta \\ \beta & 2\alpha & \beta \\ \beta & \beta & 2\alpha \end{bmatrix} \begin{bmatrix} L_1 \\ L_2 \\ L_3 \end{bmatrix} = \begin{bmatrix} F_1 \\ F_2 \\ F_3 \end{bmatrix} \quad (3.68)$$

where ψ , σ , α and β are constants.

3.4 Kinematic and dynamic models of the first prototype

A prototype of the 3RRR compliant mechanism was built, as shown in Figure 3-9.

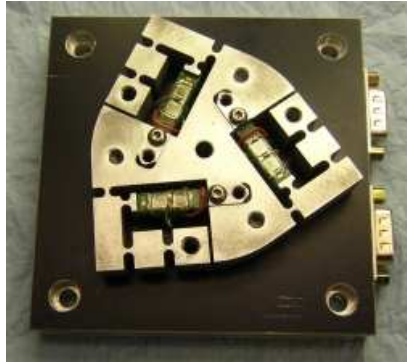


Figure 3-9 - Prototype of the 3RRR compliant mechanism.

The topology of this compliant mechanism is the same as the mechanism presented by Zhang et al. (2002). This was used for experimental verification as will be discussed in Chapter 8. The parameters of this compliant mechanism are given in Table 3-4. The end-effector was modelled as a triangle, as shown in Figures 3-7 and 3-10. The parameters defining this triangle are shown in Figure 3-10; the thickness of the triangle is $t_{\text{end-effector}}$. The material used for both the compliant mechanism and end-effector is aluminium.

3RRR Compliant Mechanism Parameter	Value
$A_2(x,y), B_2(x,y), C_2(x,y)$ (mm)	(28, 10), (23, 27), (12, 27)
T (mm)	0.94
R (mm)	1.5
B (mm)	11.7
R_0 (mm)	3.5
$cmAB_2(x,y), cmBC_2(x,y)$ (mm)	(28, 21), (17.5, 27)

b_{AB2}, h_{AB2} (mm)	22, 7
b_{BC2}, h_{BC2} (mm)	10, 8
Triangular End-Effector Parameters	Value
b_{ee} (mm)	51.18
h_{ee} (mm)	44.32
t_{end-effector} (mm)	10
Material Properties of 7075-T6 Aluminium	Value
E (MPa)	72
ρ (Kg/m³)	2810

Table 3-4 – Parameters of 3RRR compliant mechanism prototype.

These parameters were substitute into the analytical model to derive the kinematic model and dynamic model.

3.4.1 Kinematics of The first prototype

The resulting kinematic model matrix is given in equation (3.69) below.

$$\begin{bmatrix} \Delta X \\ \Delta Y \\ \Delta \theta_z \end{bmatrix} = \begin{bmatrix} -1.619 & 3.238 & -1.619 \\ 2.804 & 0.000 & -2.804 \\ -59.96 & -59.96 & -59.96 \end{bmatrix} \begin{bmatrix} \Delta L_1 \\ \Delta L_2 \\ \Delta L_3 \end{bmatrix} \quad (3.69)$$

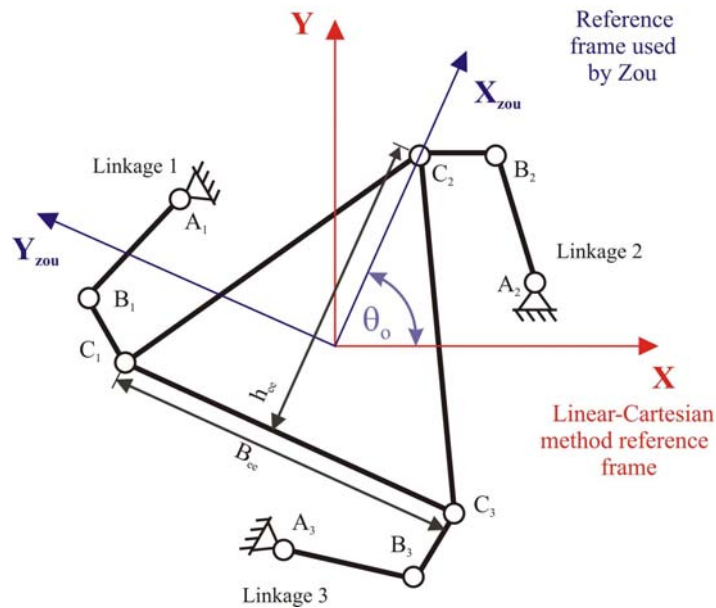


Figure 3-10 - Schematic showing the coordinate reference frame used to define the joint locations in the ‘linear-Cartesian’ method and the reference frame used by Zou (2000). The triangular end-effector parameters are also defined.

This result can be compared with the constant kinematics derived for this compliant mechanism by Zou (2000) and Yong et al. (2004). Those results used a different reference frame to define the mechanism, as shown in Figure 3-9. The matrix must be rotated by θ_0 to give the Jacobian in the same reference frame. The rotated Jacobian is given in equation (3.70) below.

$$\begin{bmatrix} \Delta X \\ \Delta Y \\ \Delta \theta_z \end{bmatrix} = \begin{bmatrix} -3.220 & 1.315 & 1.905 \\ -0.341 & 2.960 & -2.618 \\ -59.96 & -59.96 & -59.96 \end{bmatrix} \begin{bmatrix} \Delta L_1 \\ \Delta L_2 \\ \Delta L_3 \end{bmatrix} \quad (3.70)$$

This result agrees with the results presented by both Zou (2000) and Yong et al (2004). Both Zou and Yong based their models upon the PRBM, but used different methods to derive the kinematics.

In Chapter 4 the Jacobian will be derived using different modelling methods and compared to analytically derived Jacobian. Experimental verification will be discussed in Chapter 8.

3.4.2 Dynamics of the prototype 3RRR compliant mechanism

The resulting dynamic model is given in equation (3.71) below.

$$\begin{bmatrix} 0.900 & -0.305 & -0.305 \\ -0.305 & 0.900 & -0.305 \\ -0.305 & -0.305 & 0.900 \end{bmatrix} \begin{bmatrix} \ddot{L}_1 \\ \ddot{L}_2 \\ \ddot{L}_3 \end{bmatrix} + \begin{bmatrix} 3.07e7 & 7.676e5 & 7.676e5 \\ 7.676e5 & 3.07e7 & 7.676e5 \\ 7.676e5 & 7.676e5 & 3.07e7 \end{bmatrix} \begin{bmatrix} L_1 \\ L_2 \\ L_3 \end{bmatrix} = \begin{bmatrix} F_1 \\ F_2 \\ F_3 \end{bmatrix} \quad (3.71)$$

It can be noted that both the inertia and stiffness matrix are symmetrical, which is expected due to the symmetrical design of the compliant mechanism.

3.4.2.1 Natural frequencies of the prototype 3RRR compliant mechanism

The natural frequency of a system can be calculated from the mass and stiffness terms given by the dynamic model using the following eigenvalue equation.

$$|K - \omega^2 M| = 0 \quad (3.72)$$

The positive square roots of the solutions of the above equation are the natural frequencies of the system.

For the 3RRR compliant mechanism the natural frequencies are estimated theoretically from the linear dynamic model, which has the general form given in equation (3.73).

$$\begin{bmatrix} m_z & m_i & m_i \\ m_i & m_z & m_i \\ m_i & m_i & m_z \end{bmatrix} \begin{bmatrix} \ddot{L}_1 \\ \ddot{L}_2 \\ \ddot{L}_3 \end{bmatrix} + \begin{bmatrix} k_z & k_i & k_i \\ k_i & k_z & k_i \\ k_i & k_i & k_z \end{bmatrix} \begin{bmatrix} L_1 \\ L_2 \\ L_3 \end{bmatrix} = \begin{bmatrix} 0 \\ 0 \\ 0 \end{bmatrix} \quad (3.73)$$

This can also be given in the form of equation (3.74).

$$[M][\ddot{L}] + [K][L] = [0] \quad (3.74)$$

where \mathbf{M} and \mathbf{K} are the inertia and stiffness matrices, respectively, and \mathbf{L} is the input displacement vector. The Singular Value Decomposition (SVD) function in Matlab was used, as shown in equation (3.75), to determine the frequencies of the modes of vibration.

$$[U, S, V] = \text{svd}\left(\frac{K}{M}\right) \quad (3.75)$$

This function returns a diagonal matrix, \mathbf{S} , as shown in equation (3.76).

$$S = \begin{bmatrix} \omega_{n1}^2 & 0 & 0 \\ 0 & \omega_{n2}^2 & 0 \\ 0 & 0 & \omega_{n3}^2 \end{bmatrix} \quad (3.76)$$

The natural frequencies in Hz are then given by equation (3.77).

$$\omega_{ni}(\text{Hz}) = \frac{\sqrt{\omega_{ni}^2}}{2\pi} \quad (i=1,2,3) \quad (3.77)$$

The translational modes are given by ω_{n2} and ω_{n3} , while the rotational mode is given by ω_{n1} . The natural frequencies for the prototype 3RRR compliant mechanism are given in Table 3-5.

Mode	Numerical PRBM ω_n
1 st translation	793
2 nd translation	793
1 st rotation	1678

Table 3-5 - The natural frequencies predicted by the analytical PRBM for the prototype 3RRR compliant mechanism.

3.5 Discussion

The ‘linear-Cartesian’ method has been demonstrated to effectively derive the constant-Jacobian kinematic model and the linear dynamic model of the 3RRR compliant mechanism. The Jacobian derived in this study agrees with the Jacobians derived by other researchers. In Chapter 4 the kinematic model and dynamic model derived in this study will be compared to a number of models derived using other methods. In Chapter 8 experimental results will be presented to validate the models.

Chapter

4 Numerical modelling of the 3RRR compliant mechanism

In Chapter 3 an analytical pseudo-rigid-body model (PRBM) of the 3RRR compliant mechanism was presented. The PRBM of a planar compliant mechanism models a flexure hinge, as shown in Figure 4-1(a), as a revolute joint with torsional spring, joined by rigid links, as shown in Figure 4-1(b). Thus the flexure hinge has only one degree-of-freedom (DOF), rotation about the z -axis. The stiffness of this joint is given by K_b . This model has limited accuracy for predicting the kinematic and dynamic behaviour of a compliant mechanism. As discussed in Chapter 2, it has been observed by other researchers that the flexure hinges do not only undergo revolute motion but there is also translational compliance in the hinge and so the links can translate relative to each other. To model this multi-DOF behaviour using an analytical model is complex. Therefore, it is proposed to use a numerical modelling method using a Finite-Element-Analysis (FEA) package, such as ANSYS.

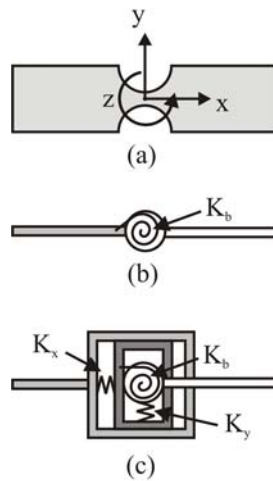


Figure 4-1 - (a) A flexure hinge, (b) a 1-DOF PRBM model and (c) a 3-DOF model.

4.1 Finite element models

In this study only planar compliant mechanisms are considered and it has been ensured that the compliant mechanisms are made from material sufficiently thick to support the z-directional load such that out-of-plane displacements are insignificant. Therefore, out-of-plane displacements can be ignored so that only translations and rotation in the x-y plane need be considered.

FEA models have been commonly used to model compliant mechanisms and have the potential to provide the most accurate prediction of the kinematic and dynamic behaviour of the compliant mechanism. A two-dimensional (2-D) Finite-Element-Model (FEM) is well suited to model planar mechanisms with uniform thickness, when there are no significant out-of-plane forces and motions. In this chapter, a 2-D FEM is presented to model the compliant mechanisms. However, to construct, mesh and solve a 2-D FEM is more time consuming and computationally expensive than a

PRBM. If multiple models need to be generated, say, for the purpose of a parametric study or optimisation, then the problem of computational expense is compounded.

It is highly desirable to find an alternative modelling method that can provide greater accuracy than a PRBM but which is computationally simple enough to be efficient for optimisation. This chapter also presents a numerical method to model a flexure hinge compliant mechanism with greater accuracy than a PRBM, while being far simpler than a 2-D FEM. The method is similar to the PRBM approach but models the flexure hinge as a joint with 3-DOF – rotation about the z-axis, and translation in x- and y-axis, as shown in Figure 4-1(c). The stiffness of this joint is described using three terms K_b , K_x and K_y , and also incorporates link compliance. This method has been termed, by the author, the Simple-Compliant-Hinge Model (SCHM).

In this chapter the FEM, SCHM and PRBM methods will all be compared. Models of a single flexure-hinge, a compliant 4-bar linkage and a 3RRR compliant mechanism are constructed using each method. The kinematic and/or dynamic model predictions are then compared. The kinematics can be compared by providing a displacement at the input location of the mechanism and then measuring the displacement at the output location. The dynamics can be compared firstly by determining the stiffness of the mechanism and secondly by determining the natural frequency of the mechanism. All the models have been created in the ANSYS environment. The PRBM constructed using ANSYS will be shown to be the same as the analytically derived model.

4.1.1 2-D Finite-Element-Model (FEM)

The 2-D FEM were constructed in ANSYS using a 2-D analysis. The models used 8-node, two-dimensional plane elements (PLANE82) with 2-DOF on each node, which are translations in the x- and y- directions. Plane-stress elements with thickness are used, as this results in a 5-10% under estimation of stiffness in the x-, y- and θ_z direction, instead of the possibility of a greater over estimation [Schotborgh et al., 2005].

A free mesh was used and to ensure a suitable mesh size a number of analysis were made using different mesh sizes. It was then checked that the output was the same each time confirming that the choice of mesh was fine enough and not causing erroneous results. The choice of loading was also carefully checked to ensure that, if point loads were used, they did not cause significant local deformation of the mesh. In some cases it was found that the load should be applied as a pressure over an area to avoid excessive local deformation within the mesh. Where ever a point load was used, the displacement needed to be measured at a point outside of the area of local deformation.

4.1.2 Simple-Compliant-Hinge Model (SCHM)

ANSYS provides the tools to construct simple models using beam, joint and spring elements. Using these types of elements it is possible to construct a PRBM type model but to incorporate more complex joint behaviour than purely revolute motion. Such a model will be discussed here. The flexure hinge is modelled using two

coincident nodes joined by two elements - COMBIN7 and COMBIN14. A schematic is shown in Figure 4-2.

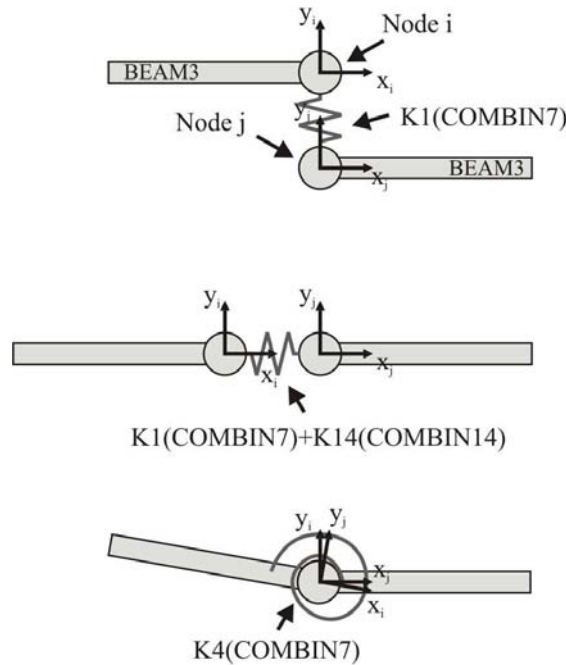


Figure 4-2- A 3-DOF model of a flexure hinge using ANSYS elements.

COMBIN7 provides a three-dimensional revolute joint with joint flexibility. The nodes (I, J) are defined to have six degrees of freedom. The DOF are defined by a local coordinate system which is affixed to each node. In this model the coordinate systems of the two coincident nodes have the same orientation. All of these DOF are intended to be constrained with a certain level of flexibility. This level of flexibility is defined by four input stiffnesses; K1 is the translational stiffness in the x-y plane, K2 is the stiffness in the z-direction; K3 is the rotational stiffness about the x- and y-axis; and K4 is the rotational stiffness in the primary degree of freedom, rotation about the z-axis, ROTZ. The dynamic behaviour of ROTZ can also be controlled using other input values, but this is unnecessary for our model. Whenever the link is

designed to have no compliance in one of these axes the stiffness is set to 10^{18} . Theoretically, to ensure no compliance the stiffness should be infinite, but this is impossible to compute. The stiffness value chosen, 10^{18} , is the largest value that can be used without causing computational problems in ANSYS. For the 3-DOF flexure hinge model the out-of-plane stiffness, K_2 and K_3 , are set to 10^{18} . COMBIN7 provides the same translational stiffness in both the x- and y-axis of the x-y plane. However, the real flexure hinge has different stiffness in the x- and y-axes. Therefore, the COMBIN7 element by itself can not adequately model the flexure hinge. To provide a more accurate model a COMBIN14 element was added. This element is used to describe a linear spring that gives an extra stiffness, K_{14} , in the x-direction. The x-and y-axis stiffness can now be set individually to accurately represent the translational compliance of the flexure hinge. The 3-DOF hinge stiffness are given by $K_x=K_1+K_{14}$, $K_y=K_1$ and $K_b=K_4$. The flexure hinges are joined by links that are represented using BEAM3 elements. The material and geometric properties of the links can be described using this element so that the link compliance behaviour is modelled. This flexure hinge model has been termed by the author the Simple-Compliant-Hinge-Model (SCHM).

4.1.2.1 Stiffness terms

Paros and Weisbord developed analytical equations to predict the stiffness of the flexure hinges in different DOF. These equations have been adopted by researchers as the standard analytical equations. Wu and Lobontiu developed simpler equations that produced the same prediction as Paros and Weisbord for hinge stiffness. In this thesis the equations of Paros-Weisbord, Wu and Lobontiu are all used depending on

which equation is the simplest and most appropriate. Figure 4-3 shows the definition of forces, moments, linear displacements and rotations used by Paros-Weisbord, Wu and Lobontiu to define the flexure hinge compliance terms. The corresponding stiffness terms are simply the reciprocal values of the compliance terms.

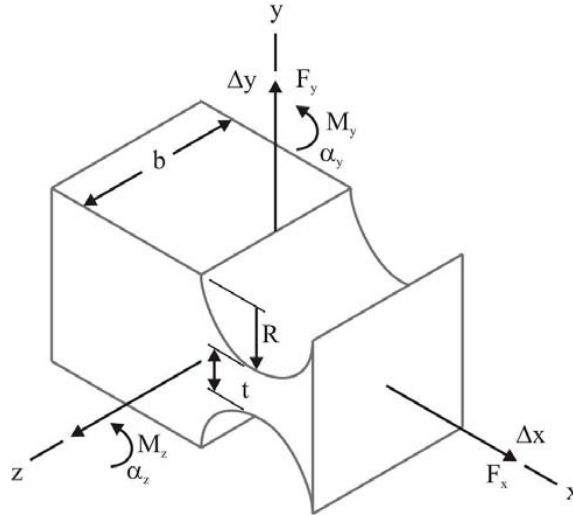


Figure 4-3- Schematic of a flexure hinge showing definition of dimensions and forces.

The equations given by Wu, equations (4.1) and (4.2) are used directly to give the stiffness terms K_b and K_x , in the SCHM.

$$\frac{1}{K_b} = \frac{\alpha_z}{M_z} = \frac{12}{EbR^2} \left[\frac{2s^3(6s^2 + 4s + 1)}{(2s + 1)(4s + 1)^2} + \frac{12s^4(2s + 1)}{(4s + 1)^{5/2}} \arctan \sqrt{4s + 1} \right] \quad (4.1)$$

$$\frac{1}{K_x} = \frac{\Delta x}{F_x} = \frac{1}{Eb} \left[\frac{2(2s + 1)}{\sqrt{4s + 1}} \arctan \sqrt{4s + 1} - \frac{\pi}{2} \right] \quad (4.2)$$

where $s = R/t$

However, K_y must be carefully determined so that it is suitable for the SCHM. As will be shown below a modification of the Paros-Weisbord equation gives an appropriate compliance value for the model. It should be noted from Figure 4-3 that F_y is applied at the edge of the hinge, a distance of R from the centre of rotation of the hinge. Therefore, the compliance term $\frac{\Delta y}{F_y}$ refers to a point R from the centre of rotation. The Δy of this point will consist of a pure y -direction translation, Δy_t and a rotational term $\alpha_z R$ as shown in Figure 4-4.

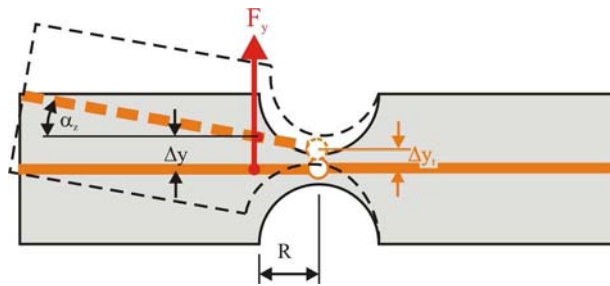


Figure 4-4- Schematic of flexure hinge and SCHM under load, showing translational displacement of hinge centre.

Δy is given by equation (4.3).

$$\Delta y = \Delta y_t + \alpha_z R \quad (4.3)$$

For the SCHM only the compliance term that defines the y -direction translation,

$\frac{\Delta y_t}{F_y}$, is needed, as the compliance is between two coincident nodes located at the

centre of rotation of the hinge. The Paros-Weisbord equation for $\frac{\Delta y}{F_y}$ in bending for a right-circular hinge is given by equation (4.4).

$$\frac{\Delta y}{F_y} = R^2 \left(\frac{\alpha_z}{M_z} \right) - \frac{3}{2Eb} \left\{ \left[\frac{1}{(1+\beta)} - \frac{2 + \frac{(1+\beta)^2}{(2\beta + \beta^2)}}{(1+\beta)} \right] + \left[\frac{4(1+\beta)}{\sqrt{2\beta + \beta^2}} - \frac{2(1+\beta)}{(2\beta + \beta^2)^{3/2}} \right] \tan^{-1} \sqrt{\frac{2+\beta}{\beta}} - \pi \right\} \quad (4.4)$$

where $\beta = t/2R$

The rotation compliance due to F_y is given by equation (4.5).

$$\frac{\alpha_z}{F_y} = R \frac{\alpha_z}{M_z} \quad (4.5)$$

Therefore, the Δy due to rotation, α_z , at distance R from the centre of rotation is given by equation (4.6).

$$\frac{\Delta y_{\alpha_z}}{F_y} = R^2 \left(\frac{\alpha_z}{M_z} \right) \quad (4.6)$$

Subtracting this term from equation (4.4) gives the y-direction translation of the centre of the hinge as given by equation (4.7).

$$\frac{\Delta y_t}{F_y} = -\frac{3}{2Eb} \left\{ \left[\frac{1}{(1+\beta)} - \frac{2 + \frac{(1+\beta)^2}{(2\beta + \beta^2)}}{(1+\beta)} \right] + \left[\frac{4(1+\beta)}{\sqrt{2\beta + \beta^2}} - \frac{2(1+\beta)}{(2\beta + \beta^2)^{3/2}} \right] \tan^{-1} \sqrt{\frac{2+\beta}{\beta}} - \pi \right\} \quad (4.7)$$

The shear compliance of the hinge is also included when calculating K_y . The equation derived by Paros-Weisbord is given in equation (4.8).

$$\frac{\Delta y_s}{F_y} = \frac{1}{Gb} \left[-\frac{\pi}{2} + \frac{2(1+\beta)}{\sqrt{2\beta + \beta^2}} \tan^{-1} \sqrt{\frac{2+\beta}{\beta}} \right] = \frac{E}{G} \frac{\Delta x}{F_x} \quad (4.8)$$

where G is the shear modulus.

Wu derived an equation that is the equivalent of the Paros-Weisbord equation, as given in equation (4.9).

$$\frac{\Delta y_s}{F_y} = \frac{1}{Gb} \left[\frac{2(2s+1)}{\sqrt{4s+1}} \arctan \sqrt{4s+1} - \frac{\pi}{2} \right] = \frac{E}{G} \frac{\Delta x}{F_x} \quad (4.9)$$

However, Lobontiu derived a different equation for shear compliance, as given in equation (4.10).

$$\frac{\Delta y_s}{F_y} = \frac{\alpha E}{G} \frac{\Delta x}{F_x} \quad (4.10)$$

where α is a correction factor that depends on the shape of the cross section. For the rectangular cross section of the single axis circular flexure hinge $\alpha = 3/2$ has been chosen, as given by [Timoshenko, 1940]. It was unclear which shear compliance was more accurate and so this needed to be studied to determine which should be used.

Finally, K_y is given by equation (4.11).

$$K_y = \frac{1}{\frac{\Delta y_t}{F_y} + \frac{\Delta y_s}{F_y}} \quad (4.11)$$

4.1.3 Pseudo-Rigid-Body-Model (PRBM)

A PRBM can easily be constructed in ANSYS. A thus defined PRBM can be used to check the numerical results of ANSYS. This is easier than a direct comparison with a standalone analytical model as everything can be done in ANSYS. In the ANSYS models the revolute joint element COMBIN7 is defined by stiffness in all 6-DOF. A pure PRBM has infinite stiffness in all DOF except for rotation about the z-axis. In the ANSYS model the PRBM was modelled by setting all stiffness values except the z-axis rotation to be 10^{18} . This value was large enough to consider any translational stiffness to be insignificant. The z-axis rotation stiffness is given by K_b . To ensure that the link deflections are negligible the BEAM3 elements are given a Young's modulus 10^4 GPa.

4.2 Flexure-hinge model

In the first investigation a single flexure-hinge was considered. The flexure-hinge is fixed at one end and connected to a rigid link at the other. Loads F_x and F_y in the x- and y- axis, of 1N, are applied independently to the end of the rigid link and the displacement and rotation of the end of the link is determined. Load F_x causes displacement Δx , while load F_y causes displacement Δy and $\Delta\theta_z$. Figure 4-5(a) shows the 2-D FEM and Figure 4-5(b) shows the equivalent SCHM / PRBM.

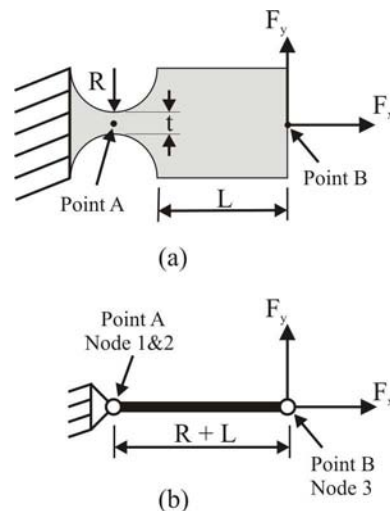


Figure 4-5- 2-D FEM model and a SCHM/PRBM of a single flexure hinge and beam.

The SCHM and PRBM models look the same but the stiffness terms are different. The load in the y-direction is applied to a single node located at the end of the beam, which did not cause significant local deformation of the mesh. However, when the x-direction load is applied as a point load significant local deformation of the mesh is caused. Therefore, the 1N load was applied as a pressure across the end of the beam.

Figures 4-6 and 4-7 present ANSYS images of a 2-D FEA model of a flexure hinge, which show the mesh, constraints and loads in the x and y directions, respectively.

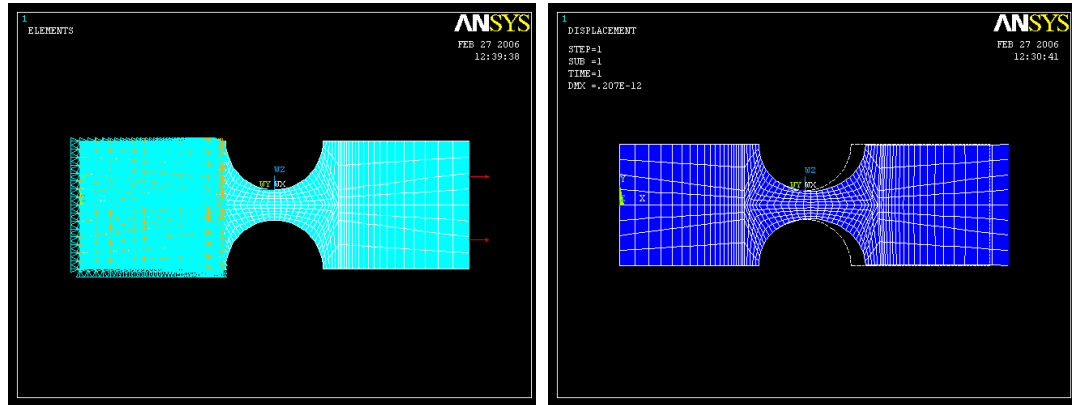


Figure 4-6- ANSYS images of a 2-D FEM of a flexure hinge. The left image shows the constraints and pressure load in the x-direction. The right image shows the (exaggerated) deformed shape of the flexure hinge.

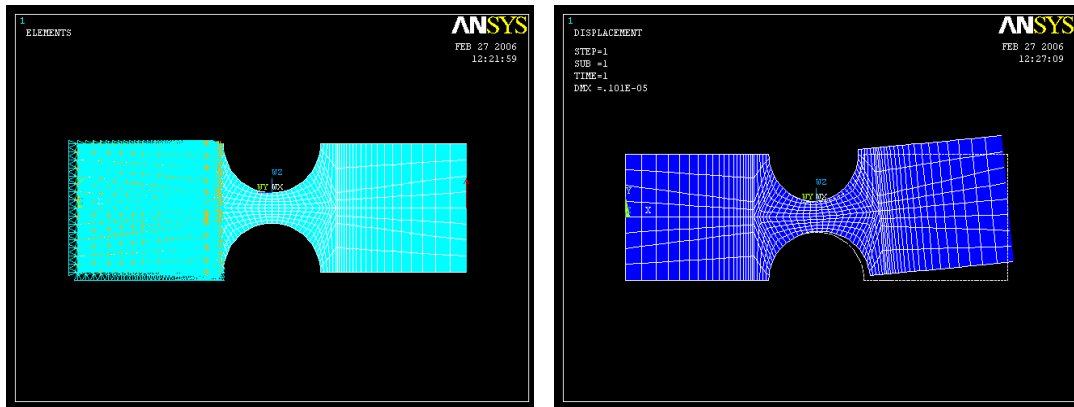


Figure 4-7- ANSYS images of a 2-D FEM of a flexure hinge. The left image shows the constraints and point force load in the y-direction. The right image shows the (exaggerated) deformed shape of the flexure hinge.

A number of flexure hinges with different hinge geometries were generated and compared. The length of the beam, $L=4\text{mm}$, hinge width, $b=10\text{mm}$ and radius of the hinge, $R=2\text{mm}$ were fixed, while the hinge thickness, t , was varied from 0.2 to 3mm.

The Young's modulus of the material was 72GPa. The displacements produced by the loads for each hinge geometry are given in Tables 4-1 and 4-2. Table 4-1 gives a comparison of the 2-D FEM and the SCHM. Table 4-2 gives a comparison of the 2-D FEM and the PRBM. As shown in equations (4.9) and (4.10) there is a choice of two possible shear compliance terms, Paros-Weisbord (PW) and Lobontiu (LOB), that can be used in calculating K_y . It was not known which of these would be more accurate and therefore both were applied and the results compared, as shown in Table 4-1.

t(mm)	2-D FEM			SCHM				% diff.			
	Δx $F_x=1N$	Δy $F_y=1N$	$\Delta\theta_z$ $F_y=1N$	Δx $F_x=1N$	Δy (PW) $F_y=1N$	Δy (LOB) $F_y=1N$	$\Delta\theta_z$ $F_y=1N$	Δx	Δy (PW)	Δy (LOB)	$\Delta\theta_z$
0.2	1.33e-8	5.75e-5	9.55e-3	1.27e-8	5.54e-5	5.54e-5	9.20e-3	4.8	3.7	3.7	3.7
0.5	8.08e-9	6.02e-6	9.94e-4	7.75e-9	5.54e-6	5.55e-6	9.15e-4	4	7.9	7.8	7.9
1	5.47e-9	1.10e-6	1.80e-4	5.27e-9	9.66e-7	9.70e-7	1.58e-4	3.7	12.3	11.9	12.3
1.5	4.20e-9	4.07e-7	6.60e-5	4.16e-9	3.48e-7	3.51e-7	5.66e-5	1	14.6	13.8	14.3
2	3.49e-9	2.01e-7	3.22e-5	3.49e-9	1.69e-7	1.71e-7	2.72e-5	-0.2	16.1	14.8	15.3
2.5	2.99e-9	1.16e-7	1.82e-5	3.04e-9	9.66e-8	9.87e-8	1.55e-5	-1.7	16.5	14.6	14.9
3	2.66e-9	7.44e-8	1.14e-5	2.70e-9	6.13e-8	6.31e-8	9.72e-6	-1.4	17.6	15.1	14.9

Table 4-1- Comparison of 2-D FEM and SCHM of single flexure hinge, and the percentage relative difference compared to the 2-D FEM. For these hinges, $R=2\text{mm}$, $b=10\text{mm}$, $E=72\text{GPa}$.

t(mm)	2-D FEM			PRBM			% diff.		
	Δx $F_x=1N$	Δy $F_y=1N$	$\Delta\theta_z$ $F_y=1N$	Δx $F_x=1N$	Δy $F_y=1N$	$\Delta\theta_z$ $F_y=1N$	Δx	Δy	$\Delta\theta_z$
0.2	1.33e-8	5.75e-5	9.55e-3	0.0	5.52e-5	9.19e-3	N/A	4.1	3.7
0.5	8.08e-9	6.02e-6	9.94e-4	0.0	5.47e-6	9.12e-4	N/A	9.0	8.2
1	5.47e-9	1.10e-6	1.80e-4	0.0	9.36e-7	1.56e-4	N/A	15.1	13.6
1.5	4.20e-9	4.07e-7	6.60e-5	0.0	3.29e-7	5.48e-5	N/A	19.3	17.0
2	3.49e-9	2.01e-7	3.22e-5	0.0	1.55e-7	2.59e-5	N/A	22.9	19.6
2.5	2.99e-9	1.16e-7	1.82e-5	0.0	8.61e-8	1.44e-5	N/A	25.5	21.0
3	2.66e-9	7.44e-8	1.14e-5	0.0	5.31e-8	8.84e-6	N/A	28.7	22.6

Table 4-2- Comparison of 2-D FEM and PRBM of single flexure hinge, and the percentage relative difference compared to the 2-D FEM. For these hinges, $R=2\text{mm}$, $b=10\text{mm}$, $E=72\text{GPa}$.

From Table 4-1 it can be seen that the relative difference between the SCHM and the 2-D FEM varies significantly depending on the flexure hinge thickness. The greatest relative difference is observed in the rotation of the hinge $\Delta\theta_z$, which increases as the hinge thickness, t , increases. The $\Delta\theta_z$ directly affects the Δy result. It can also be seen that the Lobontiu shear compliance term gives a value of K_y closer to the 2-D FEM than the Paros-Weisbord term. Assuming that the 2-D FEM gives an accurate prediction, these results suggest that the SCHM effectively models the flexure hinge behaviour. But, of course, the SCHM accuracy will be limited by the accuracy of the analytical equations, which are more accurate for some hinge geometries than for others.

It can also be seen that the SCHM is more accurate than the PRBM, particularly as t increases. For the thinnest hinge thickness, $t=0.2\text{mm}$, the PRBM is relatively accurate in predicting Δy and $\Delta\theta_z$ although it gives no indication of Δx . This indicates that for this thin hinge, and particular y -direction load case, the hinge gives close to purely revolute motion. Therefore, this suggests that the PRBM usefulness will be limited to certain cases, where the hinge design gives close to revolute motion and the loading is such that Δx is relatively insignificant. For these cases the PRBM may be able to offer appropriate accuracy. However, for general cases, where the hinge design may not give close to revolute motion and the loading causes significant Δx , the PRBM will be less accurate, and thus less useful.

4.3 Four-bar linkage

4.3.1 Stiffness

A four-bar linkage, as shown in Figure 4-8, has been modelled using the 2-D FEM, SCHM and PRBM. Input loads are applied in the x and y directions and the output displacement of the output link is determined. From these results the stiffness of the structure in the x and y direction is calculated.

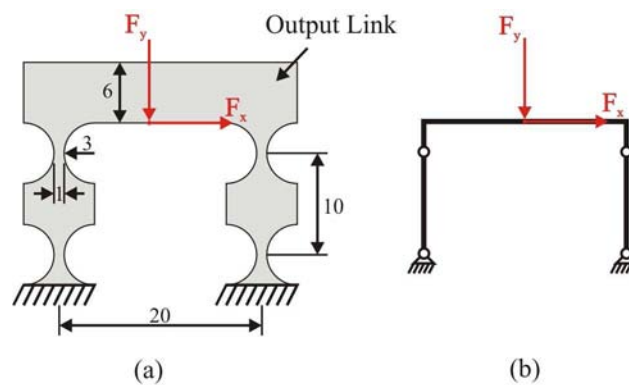


Figure 4-8- 2-D FEM and SCHM / PRBM of a four-bar linkage.

The other model parameters are:

$$b=5\text{mm}$$

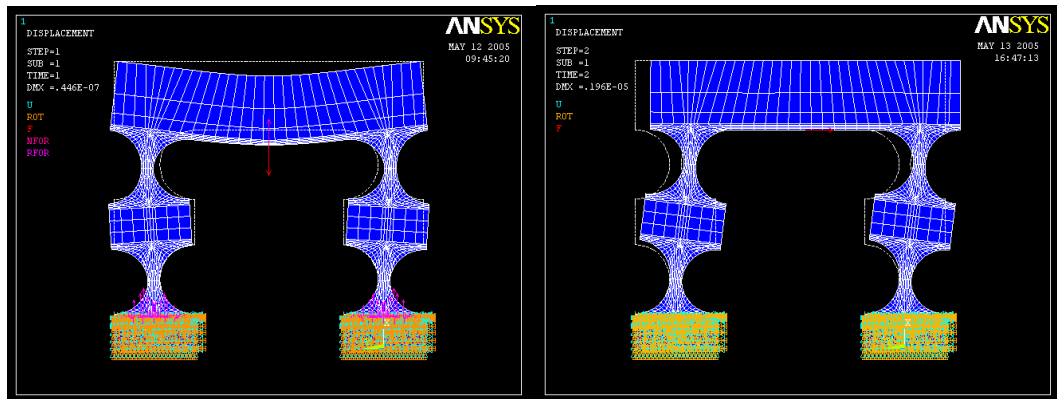
$$E=72\text{GPa}$$

$$G=27\text{GPa}$$

$$\nu=0.33$$

where b is the mechanism thickness and ν is Poisson's Ratio. The loads F_x and F_y are applied as point loads. This causes some local deformation of the FEM mesh,

particularly for F_y . Therefore, the displacement of the output link is taken from a node some distance from the force application node. It can be seen in Figure 4-9(a) that the 2-D FEM predicts that deflection of the link contributes significantly to the y-direction displacement. This suggests that, in this case, it is important for the SCHM beam elements to accurately model the compliance of the links. The x-direction load causes relatively little deformation of the links, as can be seen in Figure 4-9(b), and so modelling the link compliance is not as important for this load case.



(a)

(b)

Figure 4-9- ANSYS image showing the deformed mesh, constraints and loads applied to the four-bar FEM.

The accuracy of the flexure hinge stiffness prediction has a significant effect on the model performance. The SCHM models use values for K_x , K_y and K_b calculated using the analytical equations presented by Paros-Weisbord, Wu and Lobontiu. The values given by these equations, $K_{Analytical}$ are shown in Table 4-3. A 2-D finite-element-analysis (FEA) of this hinge geometry was conducted and these values, K_{FEA} , are also shown in Table 4-3. The percentage error between the analytical equations and the FEA is also given in Table 4-3. It can be seen that there is a

significant difference in K_b , K_x and K_y predicted by these two methods. K_b and K_x were calculated using equations (4.1) and (4.2) respectively. K_y was calculated using equations (4.7), (4.10) and (4.11). This uses the shear compliance term given by Lobontiu in equation (4.10). It is found that this shear compliance term was crucial to the accuracy of K_y . If the shear compliance term given by Paros-Weisbord or Wu, equations (4.8) and (4.9), respectively was used then K_y equalled 1.41×10^7 . The difference of this term from the FEA is 27.9%. The FEA stiffness values, K_{FEA} , are also used in the SCHM and the result compared to the model using the analytical stiffness equations.

	ANSYS 2-D FEA, K_{FEA}	Analytical Equations, $K_{Analytical}$	% diff.
K_b (Nm/rad)	13.63	15.36	12.7
K_x (N/m)	9.93E+07	1.04E+08	4.2
K_y (N/m)	1.10E+07	1.19E+07	8.3

Table 4-3- Flexure hinge stiffness terms determined from a 2-D FEA and from the analytical equations, and the percentage relative difference compared to the 2-D FEA.

The stiffness predictions for the 4-bar linkage in the x and y direction, $K_{4bar,x}$ and $K_{4bar,y}$, are shown in Table 4-4. Predictions are shown given by the 2-D FEM, SCHM and PRBM. The error of the SCHM and PRBM compared to the 2-D FEM is also shown.

	2-D FEM	SCHM				PRBM			
		$K_{analytical}$		K_{FEA}		$K_{analytical}$		K_{FEA}	
	(N/ μ m)	(N/ μ m)	% diff.	(N/ μ m)	% diff.	(N/ μ m)	% diff.	(N/ μ m)	% diff.
$K_{4bar,x}$	0.51	0.57	-12.08	0.51	0.39	0.61	-19.85	0.54	-6.35
$K_{4bar,y}$	23.94	26.56	10.94	26.22	9.52	infinite	N/A	infinite	N/A

Table 4-4- Stiffness predictions for the four-bar linkage given by 2-D FEM, SCHM and PRBM, and the percentage relative difference compared to the 2-D FEM.

It can be seen that the SCHM using $K_{\text{Analytical}}$ has a difference compared to the 2-D FEM of 12% and 11% for $K_{4\text{bar},x}$ and $K_{4\text{bar},y}$, respectively. If K_{FEA} is used then the prediction of $K_{4\text{bar},x}$ is very close to the FEM, while the prediction of $K_{4\text{bar},y}$ improves marginally. Considering $K_{4\text{bar},x}$ it can be noted that the difference of the SCHM using $K_{\text{Analytical}}$ is very close to the difference of the analytical K_b term, given in Table 4-3. This suggests that the accuracy of the SCHM under this loading condition is limited only by the accuracy of $K_{\text{Analytical}}$. However, considering the case of the y-direction load it can be noted that even when using K_{FEA} the SCHM prediction for $K_{4\text{bar},y}$ differs to the 2-D FEM by over 9%. When determining the y-direction stiffness the modelling of the rigid links is important. This suggests that there is some error in the modelling of the links.

Comparison of the SCHM and PRBM reveals that the SCHM gives a prediction of $K_{4\text{bar},x}$ that is much closer to the FEA than the PRBM, while the PRBM cannot model compliance in the y-direction at all and thus $K_{4\text{bar},y}$ is infinite.

The geometry chosen for this four-bar linkage is the same as presented in thesis of Ryu (1997) and therefore a comparison was made between those results and the results using the SCHM and 2-D FEM. Ryu's model assumed that the links were completely rigid, therefore to check those results the SCHM was given rigid links also. In Ryu's thesis the same point loads were applied to the output link in the x and y directions. The stiffness results are shown in Table 4-5 below.

	2-D FEM	SCHM		Rigid SCHM		Ryu Method		Ryu 3-D FEM	
	(N/ μm)	(N/ μm)	% diff.						
$\mathbf{K}_{4\text{bar},x}$	0.51	0.57	12.08	0.58	13.60	0.59	15.77	0.64	24.36
$\mathbf{K}_{4\text{bar},y}$	23.94	26.56	10.94	103.30	331.45	103.51	332.31	109.65	357.95

Table 4-5- Comparison Ryu's results to the 2-D FEM and the SCHM, and the percentage relative difference compared to the 2-D FEM

Considering the stiffness in the x-direction it can be seen that Ryu's method and the SCHM with rigid links predict a very similar result. The SCHM, with compliant links, predicts a slightly different result. However, Ryu's 3-D FEM and the 2-D FEM predict significantly different results. Considering the stiffness in the y-direction it can be seen that, again, Ryu's method and the SCHM with rigid links predict a very similar result. Both of these are close to Ryu's 3-D FEM. Ryu's 3-D FEM predicts even higher stiffness in the y-direction, which suggests that this model does not predict any significant compliance in the links. This prediction is very different to both the 2-D FEM and the SCHM, with link compliance. To determine which of these models provides the greatest accuracy requires experimental validation. However, this was not considered within the scope of this current work.

4.3.2 Natural frequency

A modal analysis was performed in ANSYS to determine the natural frequencies of the models. The 2-D FEM used the Block Lanczos mode extraction method to determine the first mode. The PRBM and SCHM used the reduced mode extraction method. The natural frequency predicted by the 2-D FEM, SCHM, PRBM, Ryu's Method and Ryu's 3-D FEA are given in Table 4-6 below.

	2-D FEM	SCHM		PRBM		Ryu Method		Ryu 3-D FEA	
	(HZ)	(HZ)	% diff.	(HZ)	% diff.	(HZ)	% diff.	(HZ)	% diff.
ω_n	2141.9	2060.7	3.8	2103.4	1.8	2009	6.2	2249	5.0

Table 4-6 – The natural frequency predictions given by the 2-D FEM, SCHM, PRBM, Ryu’s Method and Ryu’s 3-D FEA, and the percentage relative difference compared to the 2-D FEM.

It can be seen that the SCHM, PRBM and Ryu’s method all give similar results. An unexpected result is that the PRBM gives a result closer to the both the 2-D and 3-D FEM than either the SCHM or Ryu’s method. While Ryu’s method gives the prediction furthest from the 2-D and 3-D FEM. Ryu’s 3-D FEM and the 2-D FEM differ by 5%.

4.4 3RRR compliant mechanism

The 3RRR mechanism studied in this thesis has been modelled using the 2-D FEM, SCHM and PRBM. The geometry of the mechanism is taken from the prototype presented by Zou (2000). To simplify the model, and to give a better comparison with the experimentally determined Jacobian presented in Chapter 8, the model used here has had the input flexure hinges removed, as shown in Figure 4-10. The coordinates defining the hinge locations are given in Table 4-7. To compare the models the Jacobian, input stiffness, output stiffness and natural frequency of the models are determined.

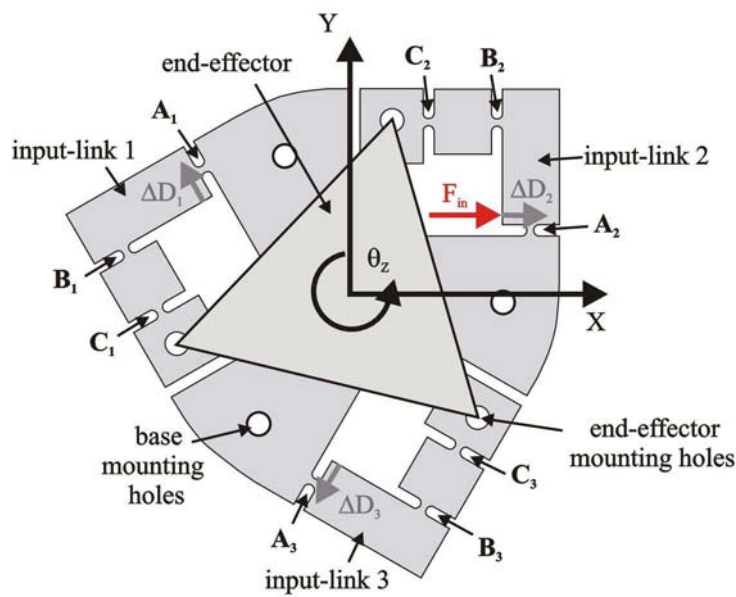


Figure 4-10- Schematic of the original 3RRR compliant mechanism (the end-effector is represented as a triangle).

Hinge	(x,y) (mm)
A ₂	(28, 10)
B ₂	(23, 27)
C ₂	(12, 27)

Table 4-7 – Coordinates defining hinge locations.

From Figure 4-10 and 4-12 it can be noted that a new term, ΔD_i ($i=1,2,3$), has been introduced. This term refers to the displacement change of the compliant mechanism, at the point where the piezo-actuator force is applied, and in the direction of the force applied by the piezo-actuator, F_{in} . The piezo-actuator input forces are applied to the input-links, which are also defined in Figure 4-10. If the displacement ΔD_i is due to an input from the i^{th} piezo-actuator, and all the piezo-actuator elongation, ΔL_i , is transferred to the i^{th} input-link, then ΔD_i equals ΔL_i . This is the assumption made in the models. However, as will be demonstrated in later sections, in the real micro-motion stage the displacement of the compliant mechanism, ΔD_i , may be different to the elongation of the piezo-actuator, ΔL_i . In other cases the displacement, ΔD_i , will be caused by coupling forces rather than the input of a piezo-actuator.

4.4.1 2-D Finite Element Model (FEM)

The 3RRR compliant mechanism, end-effector and the bolts joining them are modelled using a 2-D analysis with PLANE82 elements. The meshed ANSYS model is shown in Figure 4-11. The areas representing the bolts, as shown in Figure 4-11, are areas where the compliant mechanism, end-effector and bolts overlap. These areas are glued together, so that the compliant mechanism, end-effector and bolt nodes in these areas are fixed together. The PLANE82 elements are set to have plane-stress with thickness. The density of the compliant mechanism and end-effector elements is set to the density of aluminium. The density of the bolt elements is set such that the mass of the model bolt would equal the real mass of the bolts and spacers, which was measured. The parameters of the elements used is given in Table

4-8. It can be noted that the density used for the bolts is considerably greater than the density of the other elements, which indicates the importance of measuring their mass and accounting for this.

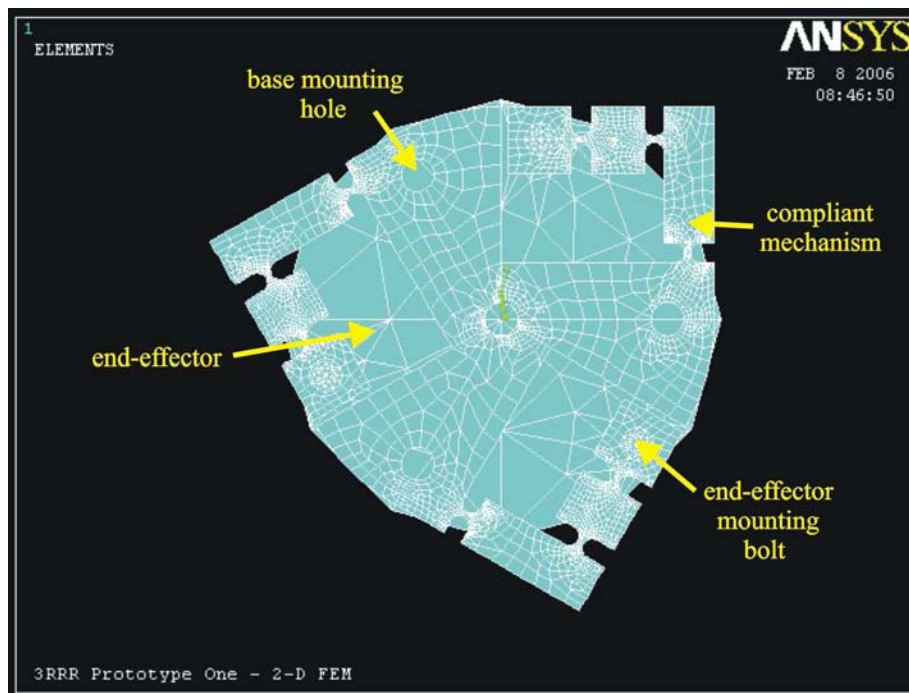


Figure 4-11- ANSYS image of meshed 2-D FEM of the 3RRR compliant mechanism, end-effector and bolts.

A free mesh was used to create the mesh. To ensure the mesh size was suitable a number of analysis were made using different mesh sizes. The output was the same each time confirming that the choice of mesh was suitable. The final mesh used had 15196 nodes. So that the model would be equivalent to the SCHM and PRBM the nodes at the base of hinge A were constrained to have zero degrees-of-freedom, rather than only constraining the nodes surrounding the base mounting holes.

	Compliant Mechanism	End-Effector	Mounting Bolts
Element type	PLANE82, plane stress w/ thickness	PLANE82, plane stress w/ thickness	PLANE82, plane stress w/ thickness
E (GPa)	72	72	72
G (GPa)	27	27	27
ν	0.33	0.33	0.33
Density (kg/m³)	2810	2810	13058
Thickness (mm)	11.7	6	11.7

Table 4-8 - Parameters for elements used in 2-D FEM of 3RRR compliant mechanism.

4.4.2 SCHM

A schematic diagram of the SCHM model is shown in Figure 4-12.

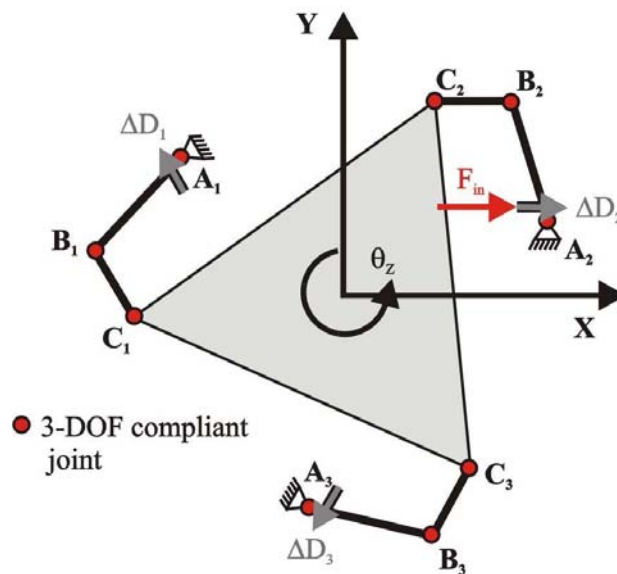


Figure 4-12- Schematic diagram of SCHM of the 3RRR mechanism.

The links of the model uses BEAM3 elements with realistic parameters, so that they model the deflection of the links as well as the hinge deflections, while the end-effector is modelled using three PLANE2 elements, as shown in Figure 4-13. The

density of the BEAM3 elements and the PLANE2 elements are set so that the model elements will have the same mass as the real components, although their volumes are different due to their different shape. The parameters used for these elements are given in Table 4-9. The flexure hinges are modelled using the same elements as described in section 4.1.2.

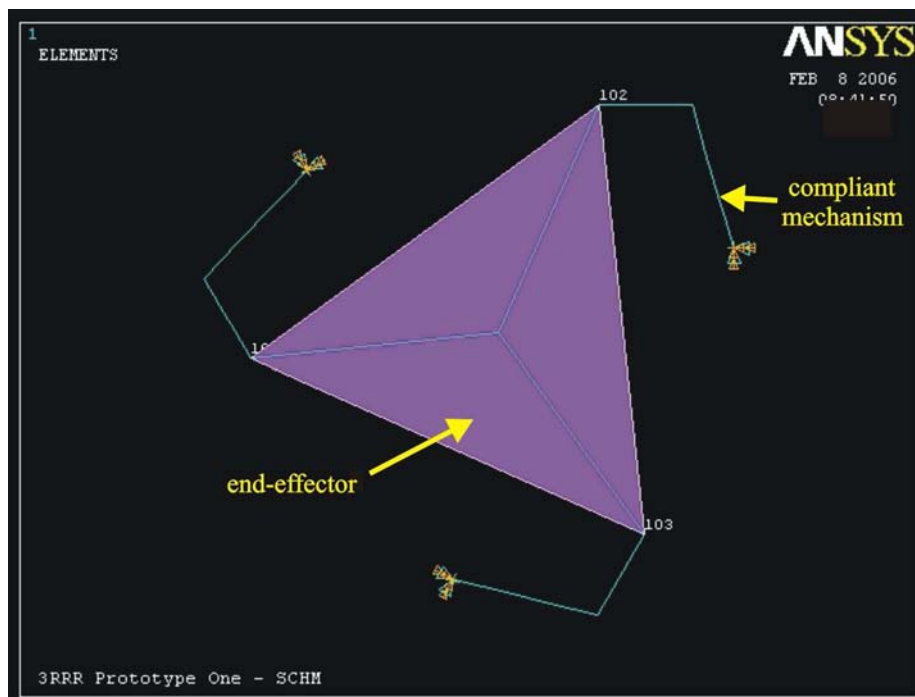


Figure 4-13 - ANSYS image of meshed SCHM of the 3RRR compliant mechanism and end-effector.

The nodes of PLANE2 elements only have 2-DOF: translations in the x and y plane. Therefore, this element cannot correctly model the rotational constraints at the corners where the links join the end-effector. To remedy this problem the corner nodes of the end-effector are also joined by BEAM3 elements, which have 3-DOF: x, y translation and rotation about the z-axis. These BEAM3 elements are set to be very rigid and have no mass.

	Compliant Mechanism		End-Effector	
	Link AB	Link BC		
Element type	BEAM3	BEAM3	PLANE2, plane stress w/ thickness	BEAM3
E (GPa)	72	72	72	1000
ν	0.33	0.33	0.33	0.33
Mass (kg)	0.0047	0.0026	0.0669	N/A
Density (kg/m³)	3255	2044	9835	0
Thickness (mm)	11.7	11.7	6	6
Width (mm)	7	10	N/A	10

Table 4-9 - Parameters for compliant mechanism links and end-effector used in the SCHM.

The accuracy of the flexure hinge stiffness prediction has a significant effect on the model performance. The SCHM model used values for K_x , K_y and K_b calculated using the analytical equations presented by Paros-Weisbord, Wu and Lobontiu. The values given by these equations, $K_{Analytical}$ are shown in Table 4-10. A 2-D FEA of this hinge geometry was conducted and these values, K_{FEA} , are also shown in Table 4-10. The percentage difference between the analytical equations and the FEA is also given in Table 4-10. It can be seen that there is a significant difference in the flexure hinge bending stiffness, K_b , predicted by these two methods, while K_x and K_y are in close agreement. K_b and K_x were calculated using equations (4.1) and (4.2) respectively. K_y was calculated using equations (4.7), (4.10) and (4.11). This uses the shear compliance term given by Lobontiu in equation (4.10). It was found that this shear compliance term was crucial to the accuracy of K_y . If the shear compliance term given by Paros-Weisbord or Wu, equations (4.8) and (4.9), respectively is used then K_y equals 7.69×10^7 . The difference to the FEA of this term is 27.5%. The FEA stiffness values, K_{FEA} , are also used in the SCHM and the results compared to the model using the analytical stiffness equations.

	ANSYS 2-D FEA, K_{FEA}	Analytical Equations, $K_{Analytical}$	% diff.
$K_b(Nm/rad)$	36.8	45.3	-23.1
$K_x(N/m)$	3.83e8	3.85e8	-0.5
$K_y(N/m)$	6.03e7	6.08e7	-0.8

Table 4-10- Flexure hinge stiffness terms determined from a 2-D FEA and from the analytical equations, and the percentage relative difference compared to the 2-D FEA.

4.4.3 PRBM

The PRBM and SCHM have the same appearance as they have the same geometry. Like the SCHM, two values of hinge stiffness K_b have been used; the value given by the analytical equations and the value given by the FEA analysis. The BEAM3 elements have E equal to 10^4 GPa, to ensure that the link deflections are insignificant.

4.4.4 Comparison of computational efficiency

The major advantage of the SCHM or PRBM models, compared to the more accurate 2-D FEM, is the shorter computation time of the simpler models, and thus better computational efficiency. To demonstrate this, the computation time of the models is compared. Table 4-11 gives the time required to build, mesh and solve each of the models. The models were all created from commands stored in text files. The solution was calculated for one static load case. The computation time to derive the dynamic model of the analytical PRBM is also given. This was derived in Matlab. The times given are the clock-time rather than the CPU time. The programs were run on a 1.8GHz Intel Pentium 4 processor.

	2-D FEM	SCHM	PRBM (Numerical)	PRBM (Analytical)
Computation Time (s)	16.9	1.8	1.8	1.7

Table 4-11 - Computation time to build, mesh and solve the 2-D FEM, SCHM and PRBM.

From Table 4-11 it can be seen that the SCHM and the two PRBM, have a similar computation time, which is far shorter than the 2-D FEM computation time. The SCHM and PRBM computation time is approximately 1/9th that of the 2-D FEM. Therefore, if the SCHM is able to give accuracy close to the 2-D FEM, it would be a far more efficient model to be used in parametric study or optimisation, where hundreds or thousands of iterations may be created.

4.5 Modelling results

4.5.1 Model Jacobians

In Chapter 3 it was demonstrated that the kinematics of the 3RRR compliant mechanism derived using the PRBM can be represented by a constant Jacobian. Such a Jacobian is shown in equation (4.12) below. It should be noted that in this equation the input displacement of the compliant mechanism, ΔD_i , is used rather than the piezo-actuator elongation, ΔL_i . The reason for this will become clear when the experimental results are presented in Chapter 8.

$$\begin{bmatrix} \Delta X \\ \Delta Y \\ \Delta \theta_z \end{bmatrix} = \begin{bmatrix} J_{11} & J_{12} & J_{13} \\ J_{21} & J_{22} & J_{23} \\ J_{31} & J_{32} & J_{33} \end{bmatrix} \begin{bmatrix} \Delta D_1 \\ \Delta D_2 \\ \Delta D_3 \end{bmatrix} \quad (4.12)$$

Using the ANSYS models the constants that fill this Jacobian are determined using the following investigative procedure. Each input-link is displaced independently by ΔD , as described in Figure 4-12, while the other two links are constrained to have zero displacement. The end-effector displacement and rotation are then recorded. Using the results from the three displacement cases the Jacobian can be filled one column at a time as shown in equation (4.13) for input-link 1.

$$\begin{bmatrix} \Delta X(\Delta D_1) \\ \Delta Y(\Delta D_1) \\ \Delta \theta_z(\Delta D_1) \end{bmatrix} = \begin{bmatrix} J_{11} & J_{12} & J_{13} \\ J_{21} & J_{22} & J_{23} \\ J_{31} & J_{32} & J_{33} \end{bmatrix} \begin{bmatrix} \Delta D_1 \\ 0 \\ 0 \end{bmatrix} = \begin{bmatrix} \Delta D_1 J_{11} + 0 + 0 \\ \Delta D_1 J_{21} + 0 + 0 \\ \Delta D_1 J_{31} + 0 + 0 \end{bmatrix} \quad (4.13)$$

The length of ΔD can be chosen arbitrarily as the Jacobian is linear and its elements are constants.

The Jacobians derived for the models are shown below. The Jacobians derived by the 2-D FEM, the SCHM and the PRBM are shown in Tables 4-12 and 4-13. In Table 4-13 the percentage relative difference between the SCHM and PRBM compared to the 2-D FEM is also given.

2-D FEM		
-1.13	2.27	-1.14
1.97	-0.01	-1.96
-41.69	-41.80	-41.77

Table 4-12- Jacobian determined using the 2-D FEM.

SCHM						PRBM					
$K_{\text{analytical}}$			K_{FEA}			$K_{\text{analytical}}$			K_{FEA}		
-1.15	2.31	-1.16	-1.22	2.45	-1.23	-1.61	3.22	-1.61	-1.61	3.22	-1.61
2.01	-0.01	-2.00	2.12	-0.01	-2.11	2.79	0.00	-2.79	2.79	0.00	-2.79
-42.77	-42.52	-42.78	-45.24	-45.02	-45.25	-59.69	-59.66	-59.69	-59.69	-59.66	-59.69
% diff. to 2-D FEM			% diff. to 2-D FEM			% diff. to 2-D FEM			% diff. to 2-D FEM		
-2.0	-2.1	-1.9	-8.0	-7.9	-7.5	-43.0	-42.2	-41.1	-43.0	-42.2	-41.1
-2.0	0.0	-2.0	-7.7	0.0	-7.8	-41.8	100.0	-42.4	-41.8	100.0	-42.4
-2.6	-1.7	-2.4	-8.5	-7.7	-8.3	-43.2	-42.7	-42.9	-43.2	-42.7	-42.9

Table 4-13- Jacobians determined using the SCHM and PRBM, and the percentage relative difference compared to the 2-D FEM.

It can be seen from the results in Table 4-13 that the SCHM using the analytical stiffness equations gives a Jacobian within 2.6% of 2-D FEM Jacobian. An unexpected, and unexplained, result is that when the FEA prediction of the flexure hinge stiffness is used, the resulting Jacobian differs to the 2-D FEM Jacobian by 7-9%. The SCHM prediction is much closer to the 2-D FEM than the PRBM, which differs to the 2-D FEM by over 40%. The PRBM Jacobian is not affected by the value of K_b .

4.5.2 Comparison with the analytically derived Jacobian

The analytically derived Jacobian, which was presented in Chapter 3, and the numerically derived Jacobian, are both shown in Table 4-14. It can be noted that the analytically and numerically derived Jacobians are almost identical.

PRBM- Jacobians					
Numerically Derived			Analytically Derived		
-1.61	3.22	-1.61	-1.62	3.24	-1.62
2.79	0.00	-2.79	2.80	0.00	-2.80
-59.69	-59.66	-59.69	-59.96	-59.96	-59.96

Table 4-14 - Comparison of numerically and analytically derived Jacobians using the PRBM for the 3RRR compliant mechanism.

4.5.3 Input stiffness

A force, F_{in} , of 1N is applied to the input-link of the models, as shown in Figure 4-10 and 4-12, and the displacement, ΔD_2 , is determined. A check was performed of the 2-D FEM that showed that the point load did not cause significant local deformation of the mesh. The load was also applied as a distributed pressure and this gave the same displacement as a point load. The input stiffness, K_{in} , is given by $K_{in} = F_{in} / \Delta D_2$. Due to the symmetry of the 3RRR mechanism the force need only be applied to one link as the other links are the same. The results for the 2-D FEM, SCHM and PRBM are shown in Table 4-15.

	2-D FEM	SCHM				PRBM			
		$K_{analytical}$		K_{FEA}		$K_{analytical}$		K_{FEA}	
		% diff.		% diff.		% diff.		% diff.	
K_{in}	1.58e7	2.04e7	-29.1	1.77e7	-12.2	3.08e7	-95.3	2.51e7	-58.8

Table 4-15- Input stiffness predicted by the 2-D FEM, SCHM and PRBM, and the percentage relative difference compared to the 2-D FEM.

From Table 4-15 it can be seen that the 2-D FEM, SCHM and PRBM give different predictions for K_{in} . The SCHM prediction is much closer to the 2-D FEM than the PRBM. The choice of K values also has a very significant effect on the result. If K_{FEA} is used then both the SCHM and PRBM give a result far closer to the FEM.

Thus the accuracy of the model is limited by the accuracy of the analytical equations used to give K_b , K_x and K_y .

4.5.4 Comparison with the analytically derived stiffness

The analytically derived PRBM stiffness matrix was presented in Chapter 3 and is shown again here.

$$K_{3RRR} = \begin{bmatrix} 3.07e7 & 7.68e5 & 7.68e5 \\ 7.68e5 & 3.07e7 & 7.68e5 \\ 7.68e5 & 7.68e5 & 3.07e7 \end{bmatrix} \quad (4.14)$$

According to this model the input stiffness is 3.07×10^7 N/m. The equivalent ANSYS PRBM predicted input stiffness was 3.08×10^7 N/m. As expected the results are nearly identical.

4.5.5 Natural frequency

A modal analysis was performed in ANSYS to determine the natural frequencies of the models. The 2-D FEM used the Block Lanczos mode extraction method, while the PRBM and SCHM used the reduced mode extraction method. The first three modes were determined. These modes correspond to two translational modes in the x-, y- plane and one rotational mode about the z-axis. Figures 4-14 to 4-16 show sequences of images taken from an animation, generated in ANSYS, of each mode of the 2-D FEM. Table 4-16 gives the natural frequencies predicted by the 2-D FEM,

SCHM and PRBM. The percentage relative difference between the SCHM and PRBM compared to the 2-D FEM is also given.



Figure 4-14 - Sequence of images from an animation generated in ANSYS of the first translational mode, 661Hz, of the 2-D FEM of the 3RRR compliant mechanism.

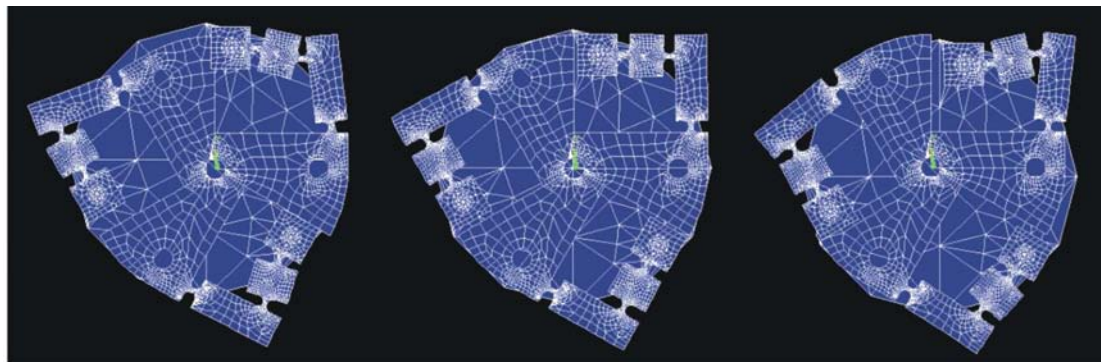


Figure 4-15 – Sequence of images from an animation generated in ANSYS of the second translational mode, 661Hz, of the 2-D FEM of the 3RRR compliant mechanism.



Figure 4-16 - Sequence of images from an animation generated in ANSYS of the first rotational mode, 1004Hz, of the 2-D FEM of the 3RRR compliant mechanism.

Comparing Figures 4-14 and 4-15, the difference between the two translational modes can be observed. They oscillate in different directions, causing different deflection of the compliant mechanism. However, both modes occur at the same frequency. This is due to the symmetry of the compliant mechanism. From Figure 4-16 the rotational mode can be clearly observed. The SCHM and PRBM experience the same modes of vibration as the 2-D FEM, but at different frequencies.

Mode	2-D FEM ω_n	SCHM				PRBM			
		$K_{\text{analytical}}$		K_{FEA}		$K_{\text{analytical}}$		K_{FEA}	
		ω_n	% diff	ω_n	% diff	ω_n	% diff	ω_n	% diff
1st translation	661	771	-16.7	697	-5.6	784	-18.7	707	-7.0
2nd translation	661	771	-16.7	697	-5.6	784	-18.7	707	-7.0
1st rotation	1004	1614	-60.7	1458	-45.2	1633	-62.6	1472	-46.6

Table 4-16 - Translational and rotational mode natural frequencies in Hz predicted by the 2-D FEM, SCHM and PRBM, and the percentage relative difference compared to the 2-D FEM.

From Table 4-16 it can be seen that the SCHM and PRBM predict similar natural frequencies, differing by only 2%, while these predictions are significantly different to the 2-D FEM prediction, particularly for the prediction of the rotational mode. The choice of K values has a significant effect on the result. If K_{FEA} is used then both models give a result far closer to the FEM, as the accuracy of the model is limited by the accuracy of the analytical equations used to give K_b , K_x and K_y . The difference between the rotational mode of the 2-D FEM and SCHM/PRBM can be attributed to the inaccurate modelling of the end-effector. The mass distribution of the circular end-effector used in the FEM is significantly different to the triangular end-effector used in the SCHM and PRBM, which is used as a simple approximation of the real end-effector.

These results suggest that either a SCHM or PRBM could be used to give a prediction of natural frequency close to the 2-D FEM, provided that the mechanism and end-effector topology are accurately modelled.

4.5.6 Comparison with the analytically derived natural frequency

The natural frequencies calculated using the analytical PRBM of the 3RRR compliant mechanism was given in Chapter 3, and is given again in Table 4-17. The natural frequency prediction given by the numerical PRBM, using $K_{\text{analytical}}$, is also given again in Table 4-17. It can be seen that the two methods predict very similar results.

Mode	Analytical PRBM ω_n	Numerical PRBM ω_n	% diff
1 st translation	784	793	1.1
2 nd translation	784	793	1.1
1 st rotation	1633	1678	2.8

Table 4-17 - Natural frequencies predicted by the numerical and analytical PRBM, and the difference between them.

4.6 Static-Coupling

Coupling describes the interference between actuators caused by the transmission of forces through the mechanism from one input-link to another. This can cause complication of the control system as the actuators are not independent. To determine the degree of coupling a force, F_{in} , is applied to input-link 2, causing displacement of all links of the mechanism, as shown in Figure 4-17. The displacement of the input-links at the point of piezo-actuator contact is given by ΔD_i

($i=1,2,3$). The couplings between input-link 1 and 2, and input-link 3 and 2, are given respectively by equations (4.15) and (4.16).

$$\text{Coupling } 1/2 = \Delta D_1 / \Delta D_2 \quad (4.15)$$

$$\text{Coupling } 3/2 = \Delta D_3 / \Delta D_2 \quad (4.16)$$

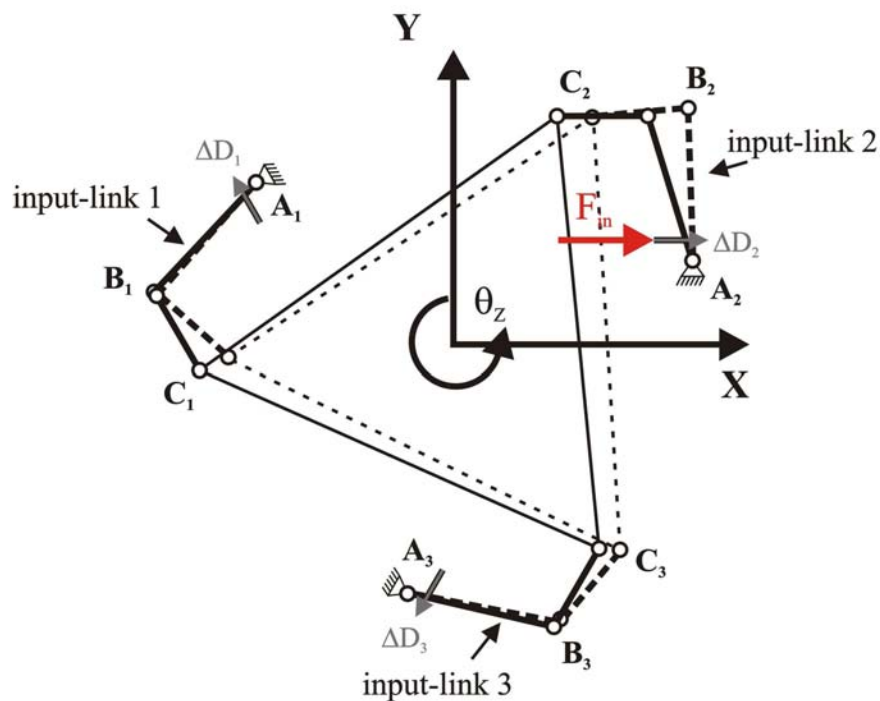


Figure 4-17 - Schematic showing coupling between input links.

In this study coupling will only be determined for a static load case and therefore the resulting coupling is termed static-coupling. The static-coupling for the 3RRR compliant mechanism is given in Table 4-18.

	2-D FEM	SCHM			PRBM		
		$K_{\text{analytical}}$ % diff.	K_{FEA} % diff.	K_{FEA} % diff.	$K_{\text{analytical}}$ % diff.	K_{FEA} % diff.	K_{FEA} % diff.
Static-Coupling 1/2	-0.010	-0.010 -4.0	-0.012 -22.5	-0.024 -144.7	-0.024 -144.8	-0.024 -144.8	
Static-Coupling 3/2	-0.010	-0.010 -4.0	-0.012 -22.5	-0.024 -144.7	-0.024 -144.8	-0.024 -144.8	

Table 4-18 - Static-coupling for the 3RRR compliant mechanism predicted by the 2-D FEM, SCHM and PRBM.

From Table 4-18 it can be observed that static-coupling 1/2 and 3/2 are identical. This is due to the symmetry of the compliant mechanism. It can also be observed that the 2-D FEM and SCHM using $K_{\text{analytical}}$ predict similar static-coupling. However, the result predicted by the SCHM when using K_{FEA} is significantly different to the 2-D FEM, which is unexpected. The PRBM predicts static-coupling that is significantly different to the 2-D FEM, and is almost unaffected by the use of $K_{\text{analytical}}$ or K_{FEA} .

4.6.1 Comparison with the analytically derived static-coupling

From inspection of the analytically derived stiffness matrix given in equation (4.14), it can be seen that there are non-diagonal terms in the matrix. These are the coupling terms. To determine the static-coupling the inverse of the stiffness matrix is determined, as given in equation (4.17).

$$\text{inv}(K_{3RRR}) = \begin{bmatrix} 3.26e-8 & -8e-10 & -8e-10 \\ -8e-10 & 3.26e-8 & -8e-10 \\ -8e-10 & -8e-10 & 3.26e-8 \end{bmatrix} \quad (4.17)$$

The non-diagonal terms are then divided by the diagonal terms to give the static-coupling terms, as given in equation (4.18). Due to the symmetry of the 3RRR compliant mechanism all the static-coupling terms are the same.

$$\text{Static - Coupling} = \frac{\text{inv}(K)_{\text{non-diagonal}}}{\text{inv}(K)_{\text{diagonal}}} \quad (4.18)$$

The static-coupling predicted by the analytical and numerical PRBM are given in Table 4-19. The difference between them is also given. It can be seen that both models give very similar predictions.

	Analytical PRBM ω_n	Numerical PRBM ω_n	% diff
Static-Coupling 1/2	-0.024	-0.024	-0.25
Static-Coupling 3/2	-0.024	-0.024	-0.25

Table 4-19 - Static-coupling predicted by the analytical and numerical PRBM, and the difference between them.

4.7 Discussion

These results demonstrate that the SCHM can represent the kinematics and dynamics of a flexure hinge mechanism with accuracy close to a 2-D FEM. However, the SCHM accuracy is limited by the analytical equations giving the K_b , K_x and K_y terms, whose accuracy varies depending on the dimensions of the flexure hinge. The SCHM provides much improved results compared to a PRBM, particularly for the geometry of 3RRR compliant mechanism considered in this chapter. The SCHM kinematic model of the 3RRR compliant mechanism is within 1% of the 2-D FEM,

compared to over 40% difference between the PRBM and the 2-D FEM. However, a surprising result is that the SCHM using K_{FEA} stiffness terms gives a prediction 8% different to the 2-D FEM. The reason for this is unclear. The predictions for stiffness and natural frequency are much improved when the K_{FEA} terms are used. The PRBM gives very similar predictions for natural frequency as the SCHM.

The SCHM is easy to generate and very quick to solve. It takes approximately $1/9^{\text{th}}$ of the computation time of the equivalent 2-D FEM. Because of its accuracy and short computation time, the SCHM is well suited to be used in a parametric study and optimisation, which will be presented in Chapters 6 and 7, respectively.

The analytically and numerically derived PRBM have been demonstrated to be the same. The minor discrepancies between them can be attributed to small differences within the computations used to derive them.

Experimental validation of the models is discussed in Chapter 8.